TECHNISCHE UNIVERSITÄT MÜNCHEN
Lehrstuhl für Technische Chemie 2

Dry Reforming of Methane – understanding metal support interactions and evaluation of regeneration protocols

Matthias Steib

Vollständiger Abdruck der von der Fakultät für Chemie der Technischen Universität München zur Erlangung des akademischen Grades eines

Doktor-Ingenieurs (Dr.-Ing.)

genehmigten Dissertation.

Vorsitzender: Prof. Dr.-Ing. Kai-Olaf Hinrichsen
Prüfer der Dissertation:

1. Prof. Dr. techn. Johannes A. Lercher
2. Prof. Dr.-Ing. Harald Klein

Die Dissertation wurde am 12.05.2017 bei der Technischen Universität München eingereicht und durch die Fakultät für Chemie am 19.02.2018 angenommen.

“Es kommt nicht darauf an, mit dem Kopf durch die Wand zu rennen, sondern mit den Augen die Tür zu finden.“

Werner von Siemens

Für meine Familie

Statutory Declaration

I declare that I have authored this thesis independently and that I have solely used the declared (re)sources and that I have marked all material, which has been quoted either literally or by content from the used sources. At the end of each chapter all collaborators are named and their specific contribution is addressed. Published content of this thesis is clearly marked.

_____, _____ _____

Acknowledgements

I would like to thank my advisor Johannes A. Lercher for giving me the chance to join his international research group for my PhD studies. It has been a tough and challenging time and I thank you for all your guidance, support and especially trust from your side. It was a pleasure for me to work in your group.

Special thanks to Andreas Jentys, my co-advisor, who accompanied me in several projects during my PhD work. Thank you Andy for all your time and patience in continuously supporting me with critical questions and fruitful discussions. Additionally, I would like to thank you for your time guiding me through the preparation, execution and data analysis of several beamtimes. I've really learned a lot from you! Furthermore, I would like to thank all collaborators of the BMBF ZeitKatMat project for fruitful discussions and successful cooperation: Jan-Dierk Grunwaldt and Andreas Gänzler from KIT in Karlsruhe; Ronald Frahm and Oliver Müller from Wuppertal University, Edmund Welter, Wolfgang Caliebe, Mathias Hermann and Wolfgang Drube from DESY in Hamburg. I would like to thank in special Xaver Hecht for the valuable help during the design construction as well as bug fixing of several setups. Xaver, without you no setup at TC2 would work and I would have spent a lot more time in finding the reason for several problems. Moreover, I would like to thank my former students Verena Höpfl and Florian Obergruber for their contribution to my work during their Master's studies in our group.

I thank all my colleagues and office mates namely Steffi Seibold, Uli Sanwald, Karen Schulz, Bettina Federmann, Andreas Marx, Daniel Melzer, Andreas Ehrmaier, Sebastian Müller, Lisl Hanrieder, Christoph Denk, Bo Peng, Stanislav Kasakov, Linus Schulz, Sebastian Foraita, Martina Braun, Sylvia Albersberger, Edith Berger, Yuanshuai Liu, Yu Lou, Sebastian Grundner, Kai Sanwald, Tobias Berto, Muthusamy Vishnuvarthan, Navneet Gupta, Moritz Schreiber, Marco Peroni, Takaaki Ikuno, Manuel Wagenhofer, Manuel Weber. I want to thank all my colleagues especially from the so called "Männerbüro": Peter Hintermeier, Maximilian Hahn, Felix Kirchberger and Ferdinand Vogelgsang. Thanks for being patient with me!

Last but not least I thank my parents Anneliese and Herbert for their continuous support during my studies. And of course I especially thank my wife Marta - without you I wouldn't be where I am now!

Thanks to all of you,

Matthias

Abstract

The role of the metal support interface for dry reforming of methane has been studied over supported Ni catalysts. The unique properties of zirconia lead to an efficient stabilization of small nanoparticles with enhanced metal support interface during catalysis and regeneration. Detailed examination of regeneration protocols with different gasifying agents revealed a kinetically controlled mechanism of coke removal and oxidation of the active metal and finally ensured stable operation of Ni based catalysts for methane dry reforming.

Kurzzusammenfassung

In dieser Arbeit wurde der Einfluss der Wechselwirkungen zwischen Metall und Träger an geträgerten Ni Katalysatoren untersucht. Dabei ermöglichten die besonderen Eigenschaften von ZrO_2 eine effiziente Stabilisierung kleiner Nanopartikel mit erhöhter Grenzfläche zwischen Ni und ZrO_2. Die Untersuchung unterschiedlicher Oxidationsmedien führte zur Entwicklung einer kinetisch kontrollierten Regenerierung von deaktivierten Katalysatoren und ermöglicht somit das Aufrechterhalten einer stabilen Aktivität von Ni/ZrO_2 für das trockene Reformieren von Methan.

Table of contents

List of figures

List of tables

Abbreviations

Symbols

c	Concentration
CSTR	Continously stirred tank reactor
d	Length
D	Dispersion
ΔH	Reaction enthalpy
DFT	Density functional theory
DRM	Dry reforming of methane
E_0	Inner potential
EXAFS	Extended X-ray absorption fine structure
FT	Fourier transformed
GHSV	Gas hourly space velocity
I	Photon intensity after the sample
I_0	Photon intensity before the sample
IR	Infra red
K	Tensile strength
k	Wavevector
k	Rate constant
μ_i	Absorption coefficient
M	Molar mass
N	Coordination number
n	Molar amount
ω	Mass fraction
p	Pressure
PFR	Plug flow reactor

$\dot{Q}$	Heat flux
QEXAFS	Quick - extended x-ray absorption fine structure
R	Distance
r	Rate
ρ	Density
s	Safety factor
σ^2	Debye waller factor
T	Temperature
TGA	Thermogravimetric analysis
TOF	Turnover frequency
TPO	Temperature programmed oxidation
TPR	Temperature programmed reduction
X	Conversion
XANES	X-ray absorption near edge structure
XAS	X-ray absorption spectroscopy

Units

Å	Angstrom
at.%	Atom percent
eV	Electron volt
Hz	Hertz
keV	Kilo electron volt
MW	Mega watt
m/z	Mass to charge
vol.%	Volume percent
wt.%	Weight percent

1 Introduction

1.1 Syngas – general background

Syngas is one of the major base chemicals produced worldwide. In 2004 the worldwide capacity of syngas production was more than 70 000 MW thermal output which was produced from a broad variety of carbon sources as depicted in Figure 1.1.[4]

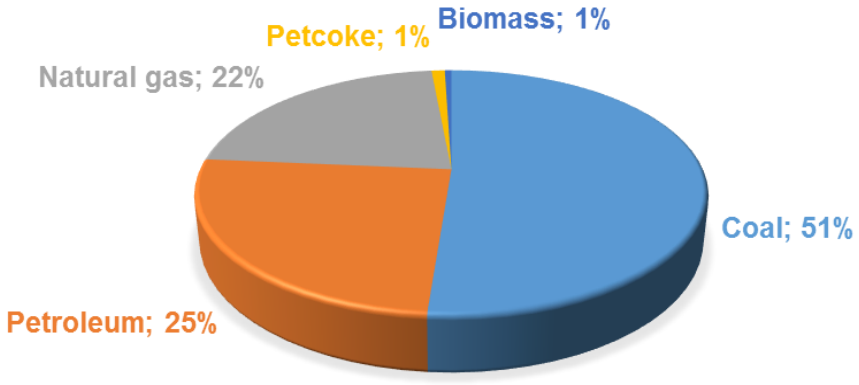

Figure 1.1: Sources of syngas in 2010. Data from [4].

Syngas production from coal is approximately 51% of the total capacity, followed by petroleum (including fuel oil, refinery residue and naphtha) with 25% and natural gas with 22%. Around 45% of the worldwide syngas production is further converted into chemicals, whereas 38% is processed to liquid fuels. Other products are gaseous fuels with approximately 6% and power generation with 11%. Syngas production technologies can efficiently utilize energy, supply clean fuels and significantly decrease the emissions of greenhouse gases. Additionally, syngas production can contribute to more efficient generation of power via coal-based Integrated Gasification Combined Cycle (IGCC) and syngas-based high temperature fuel cells (SOFCs).[5] Besides power generation syngas acts as a raw material for many chemicals such as methanol, ammonia, diesel fuels or synthetic gasoline (Fischer-Tropsch process) as depicted in Figure 1.2.[2]

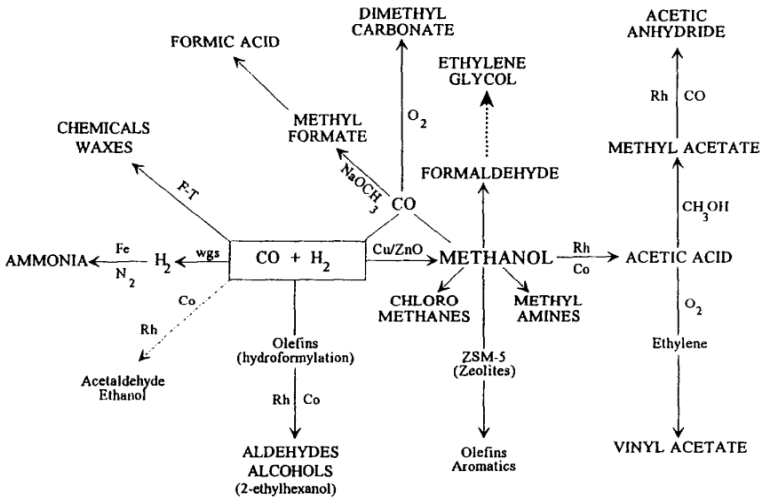

Figure 1.2: Chemical conversion routs of syngas.

Due to the H_2/CO ratio close to 1, syngas generated via methane dry reforming is suitable for the direct synthesis of aldehydes[6] and alcohols[7, 8] or gasoline synthesis by Fischer-Tropsch synthesis.[3, 6, 7]

1.2 Reforming processes

There is a broad variety of requirements for syngas with respect to pressure and H_2/CO ratio due to varying downstream processes in a refinery. Therefore, multiple techniques have been developed to produce syngas with different H_2/CO ratios.[3]

1.2.1 Steam reforming

Today steam reforming is the major source of H_2 in industry.[2] The process of steam reforming generates, depending on the feed gas composition, syngas with a H_2/CO ratio of 2.2 to 4.8. Steam reforming is mostly conducted with methane as a carbon source as methane is available worldwide and relatively cheap. Besides methane heavier hydrocarbons like naphtha are also used in this process.[9, 10]

$$CH_4 + H_2O \rightleftharpoons 3\,H_2 + CO \qquad \Delta H^0 = +206\ kJ \cdot mol^{-1} \qquad (1.1)$$

Syngas production via steam reforming of methane is a highly endothermic process which industrially proceeds via two steps, the reforming reaction itself (Equation 1.1) and the Water Gas Shift reaction (Equation 1.2), which increases the H_2 content in the synthesis gas.

$$CO + H_2O \rightleftharpoons CO_2 + H_2 \qquad \Delta H^0 = -41\ kJ \cdot mol^{-1} \qquad (1.2)$$

Before using natural gas as feed for steam reforming, sulfur containing species must be removed and kept below 1 ppmw, as sulfur can poison the catalyst.[2] In industrial scale, steam reforming is carried out at 500°C to 900°C and a pressure above 20 bar. To avoid formation of carbon deposits, the steam to carbon ratio has to be adjusted to around 2.5 as this suppresses formation of carbon deposits thermodynamically (see below). If hydrogen is the desired product of steam reforming, the gas stream of the reformer and the shift reactor has to be purified in a Pressure Swing Adsorption (PSA) unit to remove H_2O and CO_2.

1.2.2 (Catalytic) Partial Oxidation

In contrast to the endothermic steam reforming of methane, (catalytic) partial oxidation of methane (Equations 1.3 – 1.6) is an exothermic process leading to a H_2/CO ratio close to 2.

$$2\,CH_4 + O_2 \rightleftharpoons 4\,H_2 + 2\,CO \qquad \Delta H^0 = -36\ kJ \cdot mol^{-1} \qquad (1.3)$$

$$\frac{1}{4}\quad CH_4 + 2\,O_2 \rightleftharpoons CO_2 + 2\,H_2O \qquad \Delta H^0 = -800\ kJ \cdot mol^{-1} \qquad (1.4)$$

$$\frac{1}{2}\quad CH_4 + H_2O \rightleftharpoons 3\,H_2 + CO \qquad \Delta H^0 = +206\ kJ \cdot mol^{-1} \qquad (1.5)$$

$$\frac{1}{4}\quad CH_4 + CO_2 \rightleftharpoons 2\,H_2 + 2\,CO \qquad \Delta H^0 = +247\ kJ \cdot mol^{-1} \qquad (1.6)$$

The partial oxidation of methane is a combination of three reactions. In the initial stage of the reactor methane is fully oxidized to CO_2 and H_2O. The reaction products of the first stage serve as educts for the second stage, the combined steam and CO_2 reforming, whereas the heat necessary for the endothermic reforming processes is partially generated by the exothermic total oxidation in the first stage. For the partial oxidation of methane without a catalyst, reaction temperatures of 1100°C to 1500°C are necessary, whereas the usage of a catalyst reduces the required reaction temperature to around 800°C (Figure 1.3). The disadvantage of partial oxidation of methane is the high purity of oxygen which increases the costs and decreases the economic feasibility of the process.[11]

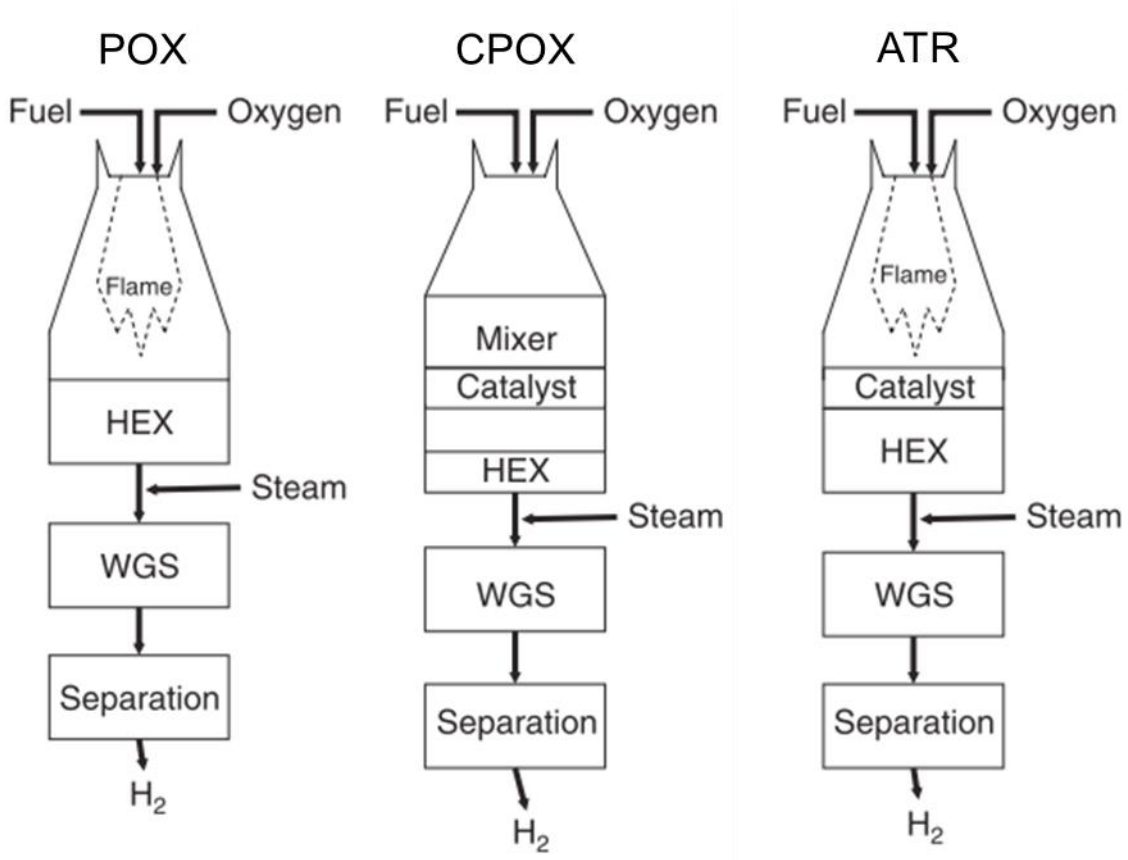

Figure 1.3: Schematic representation of the process design of partial oxidation (POX), catalytic partial oxidation (CPOX) and autothermal reforming (ATR) followed by a heat exchanger (HEX) and a water gas shift reactor (WGS), adapted from [2].

A third route to produce syngas is autothermal reforming, which is a combination of steam reforming and partial oxidation. The heat necessary for the steam reforming process is generated by the first stage total oxidation. Steam is added in a second stage to prevent coke formation. Depending on the amount of steam and oxygen, the H_2/CO ratio can vary from 1.8 to 2.5. An autothermal reformer is usually operated at reaction temperatures of 900°C to 1500°C and in a pressure range of 50 bar – 80 bar. The main advantage of the ATR process is the relatively low H_2/CO ratio, which makes the syngas favorable for downstream processes like Fischer-Tropsch or methanol synthesis.

1.3 Thermodynamic considerations

For designing and optimization of chemical processes, complete reaction networks as well as thermodynamic equilibria are discussed in this section. All calculations presented here were performed on basis of minimization of Gibbs free energy using the software package HSC Chemistry 6.0®.

1.3.1 Reaction network

In the main reaction of dry reforming of methane, CH_4 and CO_2 is converted to CO and H_2 with a theoretical H_2/CO ratio of 1 (Equation 1.7). As this reaction is strongly endothermic, high reaction temperatures of 600 – 800°C are necessary to reach acceptable conversion levels.

$$CH_4 + CO_2 \rightleftharpoons 2\,H_2 + 2\,CO \qquad \Delta H^0 = +247\ kJ \cdot mol^{-1} \qquad (1.7)$$

Besides the main reaction there are several side reactions in the reaction network of methane dry reforming. The reverse water gas shift reaction (RWGS) converts CO_2 and H_2 to CO and H_2O (Equation 1.8) and has therefore a direct influence on the H_2/CO ratio of the product gas.

$$CO_2 + H_2 \rightleftharpoons CO + H_2O \qquad \Delta H^0 = +41\ kJ \cdot mol^{-1} \qquad (1.8)$$

Water formed during the reverse water gas shift reaction can react further with CH_4 in the steam reforming reaction leading to a more hydrogen rich synthesis gas (Equation 1.9).

$$CH_4 + H_2O \rightleftharpoons 3\,H_2 + CO \qquad \Delta H^0 = +206\ kJ \cdot mol^{-1} \qquad (1.9)$$

Furthermore, there are several side reactions that involve the formation or the removal of carbon deposits. One of these reactions is the endothermic reverse Boudouard reaction (Equation 1.10), in which CO_2 reacts with carbon to form CO. Due to the high endothermicity of this reaction and the high operation temperatures of methane dry reforming, the back reaction is not favored.

$$CO_2 + C \rightleftharpoons 2\,CO \qquad \Delta H^0 = +172\ kJ \cdot mol^{-1} \qquad (1.10)$$

Another side reaction leading to the formation of carbon deposits from CO is the reverse coal gasification (Equation 1.11).

$$CO + H_2 \rightleftharpoons C + H_2O \qquad \Delta H^0 = -131\ kJ \cdot mol^{-1} \qquad (1.11)$$

The main source of carbon leading to catalyst deactivation over Ni catalysts is the endothermic methane decomposition (Equation 1.12).

$$CH_4 \rightleftharpoons C + 2\,H_2 \qquad \Delta H^0 = +75\ kJ \cdot mol^{-1} \qquad (1.12)$$

1.3.2 Effect of temperature and pressure on thermodynamic equilibria

The reaction network of methane dry reforming includes both, endothermic and exothermic reactions. Therefore, temperature has a great influence on the conversion and gas composition of the product gas (Figure 1.4).

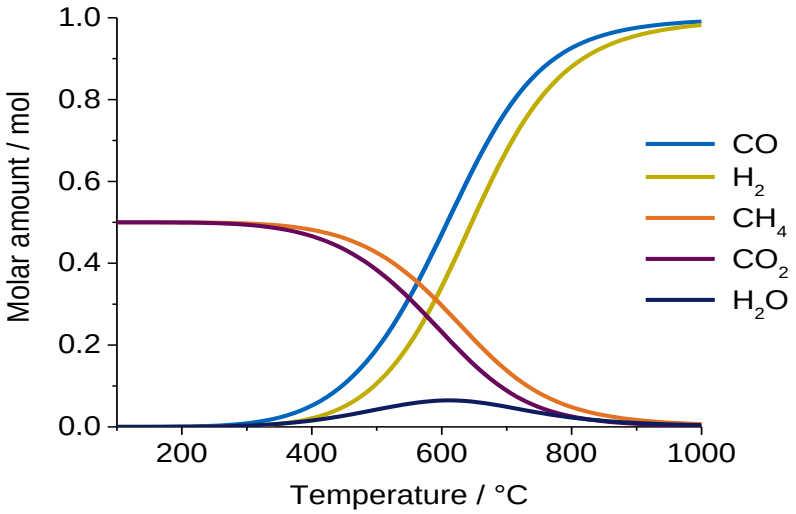

Figure 1.4: Effect of temperature on gas composition at the thermodynamic equilibrium (feed: $n_{CO2} = n_{CH4} = 0.5$ mol).

As dry reforming of methane is a highly endothermic reaction, it is conceivable that at reaction temperatures lower than 300°C, no conversion is observed. Increasing the temperature to 600°C leads to an increase of CO and H_2 in the product gas, which results from the ongoing main reaction. Please note, that the molar fraction of H_2 is always smaller than the molar fraction of CO. This is a direct consequence of the reverse water gas shift reaction, where CO_2 and H_2 are converted to CO and H_2O. Furthermore, the molar fraction of CO_2 is smaller than the molar fraction of CH_4, which is also caused by the reverse water gas shift reaction. The maximum in water partial pressure at 575°C points to the fact that at this temperature the endothermic reverse water gas shift reaction has the greatest influence on the product gas composition. At higher temperatures, the strongly endothermic steam reforming leads to a higher water consumption and thus affects an increasing H_2 production. Additionally, high temperatures suppress coke formation thermodynamically as the carbon forming reactions like the Boudouard reaction (back reaction of Equation 1.10) and the reverse coal gasification are highly exothermic processes.

High pressures are needed in industrial operation of dry reforming of methane as these high pressures are necessary to further process syngas in a refinery and compression of hydrogen is highly cost intensive compared to the compression of CH_4 and CO_2. Therefore, the following section will highlight the influence of the total pressure on the product gas composition of dry reforming of methane (Figure 1.5).

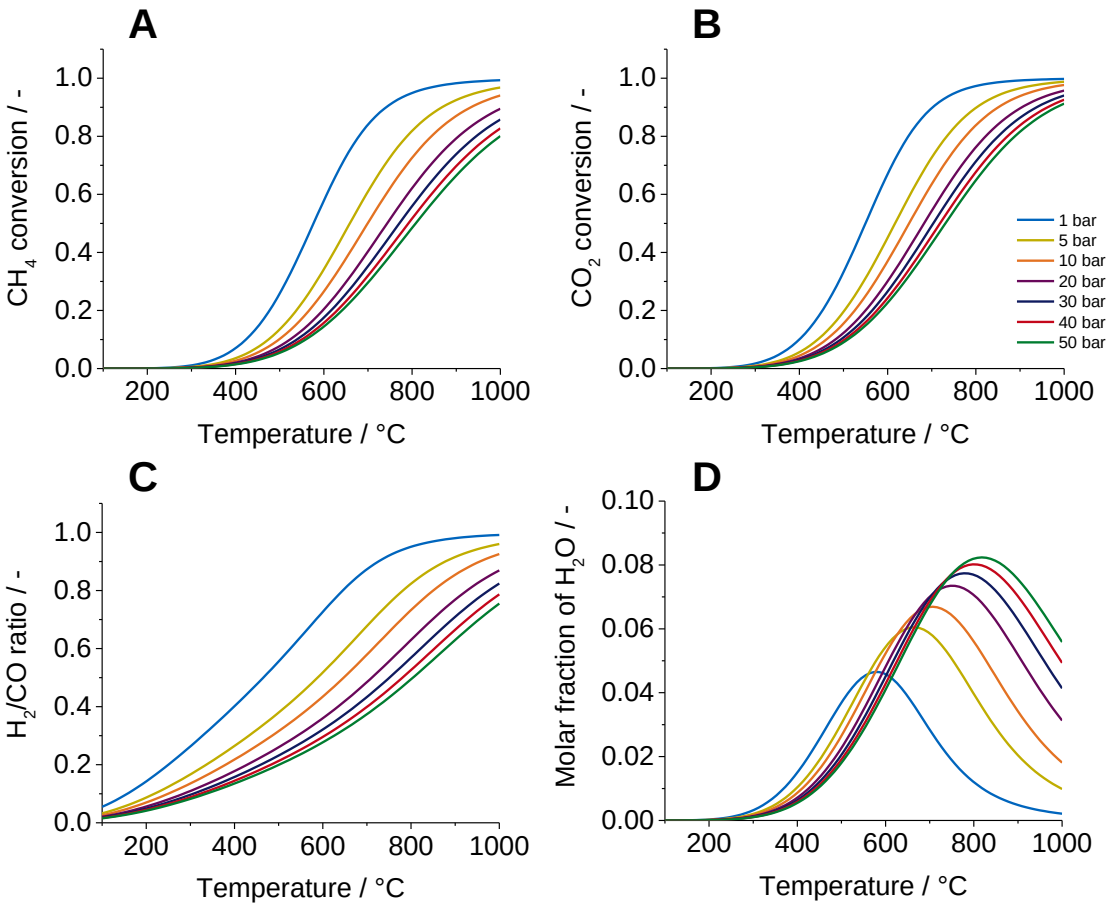

Figure 1.5: Effect of temperature and pressure on the conversion of CH_4 (A), CO_2 (B), the H_2/CO ratio (C) and the molar fraction of water (D) in the product gas.

In stoichiometric dry reforming, the total volume expands, as 2 molecules (CH_4 and CO_2) are converted into 4 (2 H_2 and 2 CO). According to Le Chatelier's principle, conversions of CH_4 and CO_2 decrease with increasing pressure. Increasing pressure decreases also the H_2/CO ratio, which shows the pressure dependency of the steam reforming reaction. At 800°C and 1 bar the theoretical H_2/CO ratio has been calculated to 0.95 whereas increasing the pressure to 50 bar leads to a decrease to 0.50.

This section showed that operation conditions can be used to control the composition of the product gas with respect to water partial pressure and H_2/CO ratio. Nevertheless, operation conditions also have a great influence on the formation of carbon deposits, which directly affect the stability of the catalyst. As coke deposition is a great challenge in methane dry reforming, the next chapter will address the influence of operation conditions on the formation of carbon deposits.

1.3.3 Carbon deposition

In addition to the overall CH_4 conversion and the desired H_2/CO ratio of the product gas, coke-free or almost coke-free operation is of great interest. Carbon deposits block the active centers of the catalyst, make them inaccessible for CH_4 and thus lead to deactivation of the catalyst. Furthermore, accumulated carbon can block the reactor tube and destroy the reactor. As mentioned, there are several endothermic and exothermic side reactions that involve the formation and the removal of carbon deposits. In the following section, the formation of carbon deposits is allowed by adding a solid phase to the calculations. Figure 1.6 shows the deposition of carbon normalized to the amount of converted carbon sources at the thermodynamic equilibrium.

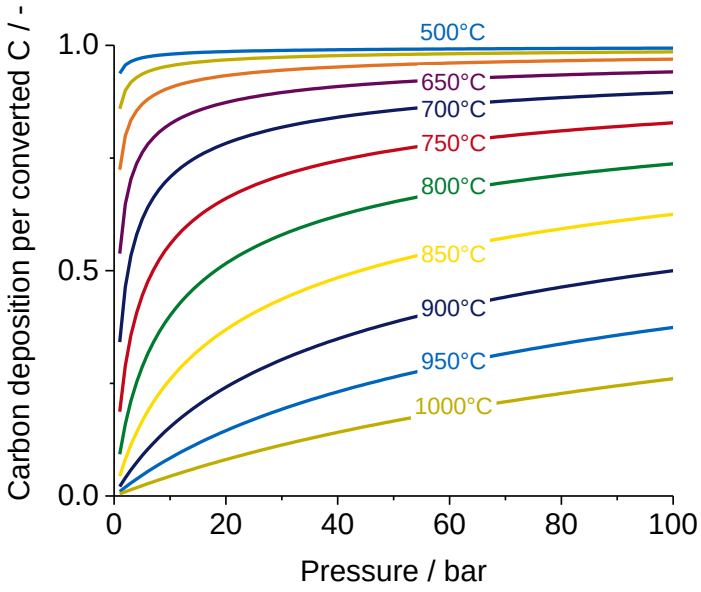

Figure 1.6: Amount of carbon per converted CH_4 as a function of pressure and temperature.

This ratio acts as a formation probability of carbon deposits and uncouples the conversion from the absolute values of carbon deposition. According to Le Chatelier's principle, carbon forming reactions are favored at high pressure. This can also be seen from Figure 1.6, as a higher operation pressure leads to increased carbon deposition. Additionally, high reaction temperatures decrease the probability of carbon formation, as two of the carbon depositing reactions are exothermic (Boudouard reaction, reverse coal gasification) and only CH_4 decomposition is endothermic. As operation conditions might be limited in temperature and pressure due to further processing of the syngas, also the influence of the feed gas composition on the thermodynamic stability of carbon deposits has to be discussed. For that purpose, calculations with varying CO_2/CH_4 ratio in the feed gas and the addition of steam (H_2O/CH_4 ratio) are examined (Figure 1.7).

To better emphasize the role of the system pressure on the stability of carbon deposits, calculations were performed for a system pressure of 1 bar and 30 bar.

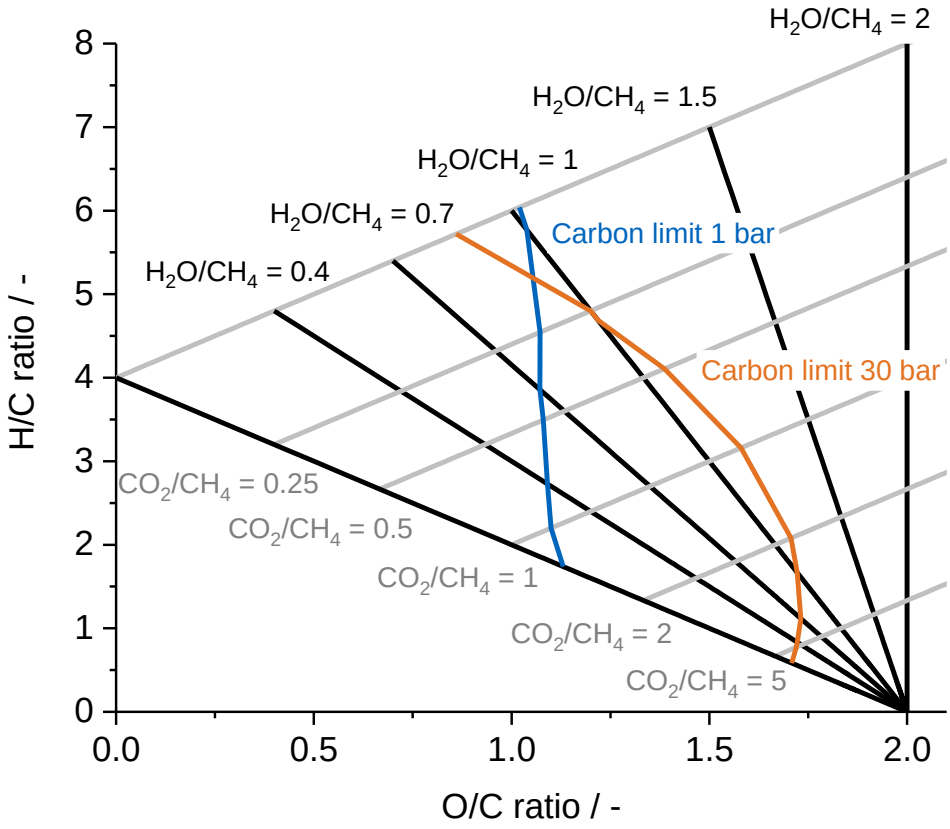

Figure 1.7: Carbon limit for dry reforming and steam reforming of methane at different pressures in dependence of the feed gas composition.

The chemical composition of the feed gas has a great influence on the thermodynamic stability of carbon deposits. A higher O/C ratio in the feed gas leads to a decreased probability of carbon formation whereas the H/C ratio has only a minor influence on the formation of carbon deposits. Please note that on the left side of the carbon limit curves in Figure 1.7, carbon formation is thermodynamically favored. At atmospheric pressure carbon deposits are stable for stoichiometric dry reforming ($CO_2/CH_4 = 1$) and steam reforming of methane ($H_2O/CH_4 = 1$). Increasing the pressure to 30 bar shifts the carbon limit curve to higher CO_2/CH_4 ratios and lower H_2O/CH_4 ratios. This makes stable operation of dry reforming of methane at elevated pressure without significant addition of water highly difficult. At atmospheric pressure, the addition of minor amounts of steam to the feed gas can already prevent coke deposition from a thermodynamic point of view. As industrial processes operate at high pressure, adjusting the feed gas composition is not an effective way to prevent carbon formation. Therefore, catalysts and general concepts have to be developed to overcome current limitations and to ensure stable operation.

1.4 Reaction mechanism

The mechanism of dry reforming of methane has been vividly investigated over the last decades with many different results as there is a broad variety of active materials for this reaction.[1, 12-14] The most accepted mechanism has been proposed by Iglesia et al. for dry reforming and steam reforming of methane over Ni and noble metal based catalysts (Figure 1.8).[1]

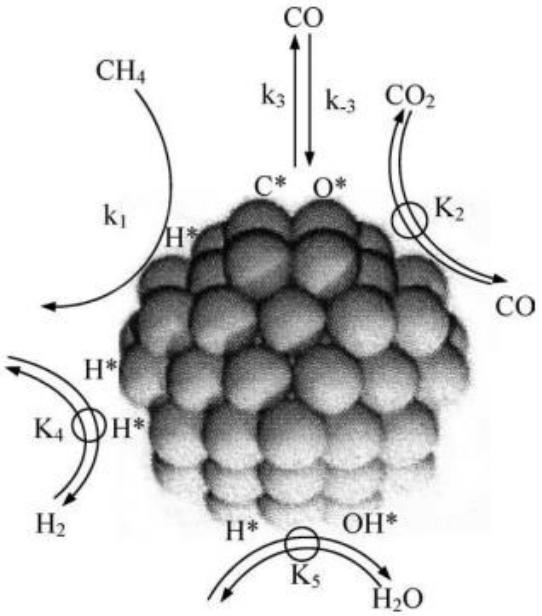

Figure 1.8: Mechanism of CH_4 reforming with CO_2 or H_2O as co-reactant as proposed by Iglesia et al.[1]

They revealed the sole influence of the CH_4 partial pressure on the overall reaction rate for dry reforming and steam reforming of methane. Transient kinetic analysis combined with isotopic labelling of reactants has been used to unequivocally proof that breaking the first C-H bond in CH_4 at the metal surface sites leading to adsorbed CH_3* and H* is the rate determining step independent of the co-reactant (CO_2 or H_2O). It is generally accepted in literature, that CH_4 is decomposed at the surface of the metal particle, whereas CO_2 can also be decomposed at the interface of the metal and the support.

Bitter et al. proposed a bifunctional mechanism for dry reforming of methane over Pt/ZrO_2 catalysts, where CH_4 is decomposed at the metal surface forming H* and CH_x* species while CO_2 is predominantly adsorbed at the metal support interface forming carbonates.[15-17] This opens an additional pathway providing oxygen species which can remove carbon deposits. It has been shown that the additional decomposition of CO_2 at the perimeter effectively removes carbon from CH_4 decomposition in the vicinity of metal and support leading to a particle which is partially covered with carbon deposits only at the metal surface.

1.5 Catalysts for dry reforming of methane

In general, catalysts for dry reforming of methane can be divided into two classes, noble metal catalysts and non-noble metal catalysts. Noble metals like Ir, Pt, Rh, Ru and Pd have excellent activity and very high stability as shown by many groups. Bradford and Vannice[18] investigated the activity of those materials for dry reforming of methane and found the sequence in activity as follows:

Ru, Rh > Ir > Ni, Pt, Pd

Iglesia et al. have shown over MgO supported catalysts that a comparison of the turnover rate is difficult as the dispersion has a great influence on the activity (Figure 1.9).[1]

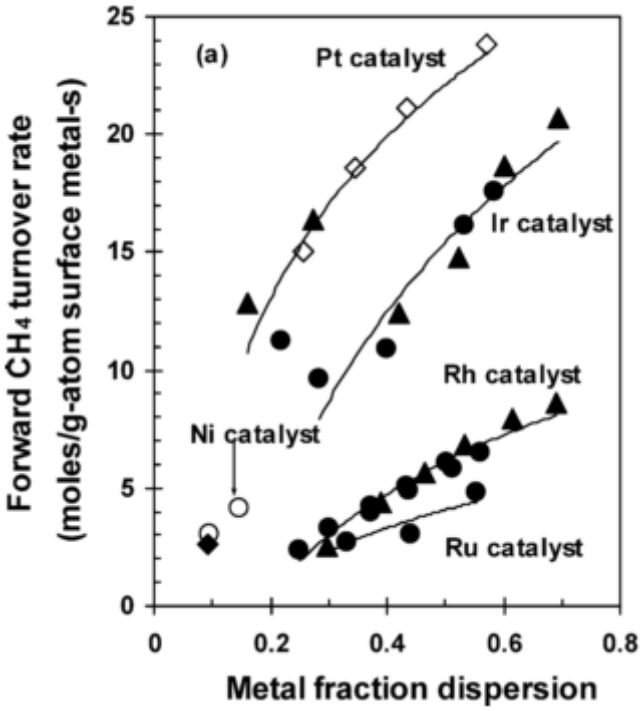

Figure 1.9: Influence of the metal dispersion on the turnover rate of methane dry reforming.[1]

This dependence could result from different reactivities of different sites at the metal surface. In this comparison, Pt is the most active metal. As reforming processes are high volumes processes in industrial scale, also large amounts of catalyst are necessary. This makes the usage of noble metal catalysts, although they are highly stable, very cost intensive and thereby economically not feasible.

Non-noble metals like Ni or Co have also good activity in methane reforming but these catalysts suffer from deactivation due to sintering and coke deposition. Therefore, current focus of research lies on the development of stable Ni and Co based catalyst systems. In literature, several attempts are described to overcome current limitations of conventional non-noble metal based catalysts, e.g. by applying new preparation methods[19-22], decreasing the particle size of the active metal[23], introducing promotors[24-28] to enhance carbon removal and the usage of bimetallic systems.[29]

While the active metal determines the overall activity in methane reforming processes, the support has implications on the stability especially for non-noble metal based catalyst. Dry reforming of methane is a strongly endothermic route, which requires high reaction temperatures of 600 – 800°C to reach acceptable conversion levels. At this high temperature the support has to stabilize metal particles against sintering. Supports widely used for catalyst design are Al_2O_3[30-34], CeO_2[35-37], TiO_2[38-40] and ZrO_2[15-17, 41-43]. Bitter et al. provided evidence for the influence of the support on the stability of reforming catalysts. They investigated Pt supported on Al_2O_3, TiO_2 and ZrO_2 whereas the stability increased in the following order:

$Pt/Al_2O_3 < Pt/TiO_2 < Pt/ZrO_2$

The unique properties of ZrO_2 to stabilize particles against sintering, to provide oxygen in the form of carbonates and to have significant Lewis acidity were found as reasons for the increased stability.

1.6 Scope of this thesis

The goal of this thesis is the development of a general approach for stable operation of Ni based catalysts for methane dry reforming at elevated temperatures. As carbon deposition is thermodynamically favored under dry reforming conditions, new concepts have to be developed to regenerate a deactivated catalyst without significantly deteriorating the overall reaction rate. The key for developing this concept is a fundamental understanding of metal support interactions as well as their influence on the activity and stability of the catalyst. To get useful information about the structure of the catalyst, characterization has to be done under reaction conditions by in situ / in operando spectroscopy.

For that purpose, the second chapter of this thesis deals with the design and construction of a novel cell for in situ X-ray absorption spectroscopy. Detailed evaluation of possible materials for the cell with respect to temperature and pressure durability and sufficient transmissibility for X-rays led to a new design of capillary cells, which makes the investigation of reactions in a wide temperature and pressure range possible. The parallel design ensures treatment of up to five samples at the same temperature with high flexibility in pressure and gas composition and allows an efficient usage of highly time limited synchrotron radiation.

In the third chapter the dynamic restructuring of Ni/ZrO_2 surfaces for methane dry reforming is studied. Kinetic measurements combined with time resolved X-ray absorption spectroscopy reveal the importance of the metal support interface in stabilizing small metal particles and in supplying labile oxygen species for the removal of carbon deposits during catalysis and regeneration. It is shown that exposing a Ni/ZrO_2 catalyst to a stream of pure CO_2 dynamically restructures the surface of the catalyst leading to a highly active catalyst for methane dry reforming.

The fourth chapter of this thesis focuses on the determination of oxidation/reduction kinetics of small nanoparticles under dry reforming conditions. Highly time resolved X-ray absorption spectroscopy is used to reveal the influence of the gasification agent (CO_2, O_2 and N_2O) on the structural properties of the metal particles during catalyst regeneration. With this knowledge, a mechanism of kinetically controlled oxidation of Ni and carbon is proposed.

1.7 Literature

1. J. M. Wei and E. Iglesia, *J. Catal.*, 2004, **224**, 370-383.
2. C. Song, *Hydrogen and Syngas Production and Purification Technologies*, Wiley New York, 2010.
3. I. Wender, *Fuel Process Technol*, 1996, **48**, 189-297.
4. C. Ampelli, S. Perathoner and G. Centi, *Philosophical Transactions of the Royal Society A: Mathematical, Physical and Engineering Sciences*, 2015, **373**.
5. L. F. Brown, *Int J Hydrogen Energ*, 2001, **26**, 381-397.
6. A. P. E. York, T. c. Xiao, M. L. H. Green and J. B. Claridge, *Catalysis Reviews*, 2007, **49**, 511-560.
7. E. S. W. Boll, G. Hochgesand, C. Higman, P. Kalteier, W.D. Müller, M. Kriebel, H. Schlichting, H. Tanz, *Ullmann's Encyclopedia of Industrial Chemistry*, Wiley-VCH, Weinheim, 2007.
8. X. D. Peng, A. W. Wang, B. A. Toseland and P. J. A. Tijm, *Ind Eng Chem Res*, 1999, **38**, 4381-4388.
9. R. F. Aguilera, *Energy*, 2010, **35**, 3332-3339.
10. D. Möst and H. Perlwitz, *Energy*, 2009, **34**, 1510-1522.
11. J. M. Ogden, E. Dennis, M. Steinbugler and J. Strohbehn, *Center for energy and environmental studies, Princeton University*, 1995.
12. V. Y. Bychkov, O. V. Krylov and V. N. Korchak, *Kinet. Catal.*, 2002, **43**, 86-94.
13. Y. H. Cui, H. D. Zhang, H. Y. Xu and W. Z. Li, *Appl Catal a-Gen*, 2007, **318**, 79-88.
14. J. Z. Luo, Z. L. Yu, C. F. Ng and C. T. Au, *J. Catal.*, 2000, **194**, 198-210.
15. J. H. Bitter, K. Seshan and J. A. Lercher, *J. Catal.*, 1998, **176**, 93-101.
16. J. H. Bitter, K. Seshan and J. A. Lercher, *J. Catal.*, 1999, **183**, 336-343.
17. J. H. Bitter, K. Seshan and J. A. Lercher, *Top Catal*, 2000, **10**, 295-305.
18. M. C. J. Bradford and M. A. Vannice, *Catal. Today*, 1999, **50**, 87-96.
19. D. Baudouin, K. C. Szeto, P. Laurent, A. De Mallmann, B. Fenet, L. Veyre, U. Rodemerck, C. Coperet and C. Thieuleux, *J Am Chem Soc*, 2012, **134**, 20624-20627.
20. S. Carenco, C. Boissiere, L. Nicole, C. Sanchez, P. Le Floch and N. Mezailles, *Chem Mater*, 2010, **22**, 1340-1349.
21. O. Metin, V. Mazumder, S. Ozkar and S. S. Sun, *J Am Chem Soc*, 2010, **132**, 1468-+.
22. J. Park, E. Kang, S. U. Son, H. M. Park, M. K. Lee, J. Kim, K. W. Kim, H. J. Noh, J. H. Park, C. J. Bae, J. G. Park and T. Hyeon, *Adv Mater*, 2005, **17**, 429-+.
23. V. M. Gonzalez-Delacruz, R. Pereniguez, F. Temero, J. P. Holgado and A. Caballero, *Acs Catal*, 2011, **1**, 82-88.
24. X. Li, J.-S. Chang, M. Tian and S.-E. Park, *Appl Organomet Chem*, 2001, **15**, 109-112.
25. J. A. Montoya, E. Romero-Pascual, C. Gimon, P. Del Angel and A. Monzón, *Catal. Today*, 2000, **63**, 71-85.
26. B. Stolze, J. Titus, S. A. Schunk, A. Milanov, E. Schwab and R. Gläser, *Frontiers of Chemical Science and Engineering*, 2016, **10**, 281-293.
27. S. A. Theofanidis, V. V. Galvita, H. Poelman and G. B. Marin, *Acs Catal*, 2015, **5**, 3028-3039.
28. A. Wolfbeisser, O. Sophiphun, J. Bernardi, J. Wittayakun, K. Föttinger and G. Rupprechter, *Catal. Today*, 2016, **277, Part 2**, 234-245.
29. D. San-Jose-Alonso, J. Juan-Juan, M. J. Illan-Gomez and M. C. Roman-Martinez, *Appl Catal a-Gen*, 2009, **371**, 54-59.
30. X. Tu, H. J. Gallon, M. V. Twigg, P. A. Gorry and J. C. Whitehead, *Journal of Physics D: Applied Physics*, 2011, **44**, 274007.
31. U. Olsbye, T. Wurzel and L. Mleczko, *Ind Eng Chem Res*, 1997, **36**, 5180-5188.

32. T. Horiuchi, K. Sakuma, T. Fukui, Y. Kubo, T. Osaki and T. Mori, *Applied Catalysis A: General*, 1996, **144**, 111-120.
33. N. A. Pechimuthu, K. K. Pant and S. C. Dhingra, *Ind Eng Chem Res*, 2007, **46**, 1731-1736.
34. J. Juan-Juan, M. Román-Martínez and M. Illán-Gómez, *Applied Catalysis A: General*, 2006, **301**, 9-15.
35. N. Laosiripojana and S. Assabumrungrat, *Applied Catalysis B: Environmental*, 2005, **60**, 107-116.
36. A. Kambolis, H. Matralis, A. Trovarelli and C. Papadopoulou, *Applied Catalysis A: General*, 2010, **377**, 16-26.
37. V. M. Gonzalez-Delacruz, F. Ternero, R. Pereñíguez, A. Caballero and J. P. Holgado, *Applied Catalysis A: General*, 2010, **384**, 1-9.
38. K. Nagaoka, K. Takanabe and K.-i. Aika, *Applied Catalysis A: General*, 2004, **268**, 151-158.
39. K. Nagaoka, K. Takanabe and K.-i. Aika, *Applied Catalysis A: General*, 2003, **255**, 13-21.
40. S. Zhang, J. Wang and X. Wang, *Journal of Natural Gas Chemistry*, 2008, **17**, 179-183.
41. J. Lercher, J. Bitter, W. Hally, W. Niessen and K. Seshan, *Studies in Surface Science and Catalysis*, 1996, **101**, 463-472.
42. J. W. Han, C. Kim, J. S. Park and H. Lee, *Chemsuschem*, 2014, **7**, 451-456.
43. S. Li, C. Zhang, Z. Huang, G. Wu and J. Gong, *Chem. Comm.*, 2013, **49**, 4226-4228.

2 Design of a parallel capillary cell for in situ X-ray absorption spectroscopy

2.1 Introduction

Investigations on the structure-activity relationship of heterogeneous catalysts gained interest in recent years as these studies are the key for advanced catalyst development. Therefore, the catalysts have to be studied in situ or in operando to simultaneously monitor the activity of a catalyst and its structural changes. For that purpose, in situ X-ray absorption spectroscopy can be used as an efficient tool to monitor structural changes under reaction conditions without affecting the catalyst itself. To record these changes parallel to the catalytic activity, in situ cells have to meet several requirements. In this work the development of a novel in situ cell, which allows the parallel treatment of up to five catalyst samples is shown. The usage of this cell drastically reduces the time necessary to obtain good data for a series of catalysts and therefore allows highly efficient usage of synchrotron radiation.

2.2 Experimental

2.2.1 X-ray absorption spectroscopy

X-ray absorption spectra were measured at the SuperXAS beamline at the SLS in Villigen. All data were recorded in transmission mode at the Ni K-edge at 8333 eV with a channel-cut Si(111) monochromator operated at an oscillation frequency of 30 Hz. Analysis of the QEXAFS data was carried out with the JAQ software.[1]

The in situ experiments were conducted in a quartz glass capillary (WJM Glas, 1 mm diameter, 10 µm wall thickness). The pressed catalysts (80 – 120 µm) were diluted with BN and the catalyst bed (4 mm length) was fixed in the capillary with two plugs made of quartz wool. The capillary was placed in the sample holder as described above. The flow of the reactant gasses during the experiment was kept constant at 10 $mL \cdot min^{-1}$.

To compare the signal quality obtained from the capillaries to a conventional pellet cell, a self-supporting wafer of the 10 wt.% Ni/ZrO_2 catalyst was prepared and placed in an oven.

2.2.2 Activity tests

The activity tests were carried out in a 4 mm plug flow reactor made of quartz glass. The catalyst was fixed between two plugs of quartz wool. Prior to reaction at 800°C the catalyst was reduced in situ at 600°C in 10% H_2 in He for 90 minutes. The reaction was carried out at ambient pressure with a reactant gas consisting of 15 vol.% CH_4 (99.995 vol.%), 15 vol.% CO_2 (99.995 vol.%) and 70 vol.% He (99.999 vol.%) with a total flow of 80 $mL \cdot min^{-1}$. The catalytic test in the capillary was carried out at identical conditions. To obtain the same space velocity the total flow was adjusted to 10 $mL \cdot min^{-1}$. The product gas was analyzed with an online mass spectrometer (Pfeiffer Omnistar GSD 320).

2.2.3 Catalyst preparation

Ni supported on ZrO_2 (Mel chemicals, XZO1501/03) was prepared with a loading of 10 wt.% by incipient wetness impregnation using an aqueous solution of nickel(II) nitrate hexahydrate (Acros, 99%) as described in detail previously.[2] After impregnation at room temperature, the catalysts were dried at 100°C for 12 h, calcined in air at 400°C for 2 h (flow rate: 100 $mL \cdot min^{-1}$) and reduced with H_2 at 400°C (heating rate of 0.5 $K \cdot min^{-1}$) for 2 h (flow rate: 100 $mL \cdot min^{-1}$).

2.3 Results and discussion

2.3.1 Cell design and state of the art

Literature describes different designs [3-12] of XAS cells for in situ/operando studies of gas phase reactions, which can be divided in general into two classes, pellet cells and plug flow cells. In the first type, a self-supporting waver is pressed out of a powder sample and placed in an oven for temperature control during the XAS experiments. The main advantage of this type of cell is the distance between the waver (together with the heating unit) and the cell windows, allowing high flexibility in choice of the window material, as the windows can be cooled externally. Therefore, high temperature (up to 600°C) are possible with windows made of kapton, while for high pressure studies windows made of Beryllium or glassy carbon have to be used. Another advantage of these pellet cells is the constant concentration of the reactant over the samples, resulting from the back mixing inside the cells. However, fast changes in the composition of the reactant atmosphere are not possible due to the residence time distribution of a CSTR.

In contrast, a capillary cell can be described as a plug flow reactor, which allows fast changes in the gas composition. Depending on operation conditions (temperature, pressure and the edge energy), different materials can be used for a capillary reactor. Dreher et al.[13] designed a plug flow reactor with a diameter of 6 mm and a wall thickness of 1.25 mm made of AlN that can withstand pressures up to 300 bar and temperatures up to 500°C for gasification of biomass in supercritical water over a Ru based catalyst. Ceramic materials such as AlN exhibit an excellent transmissibility for X-rays at high energies, whereas this kind of material is not sufficiently transparent for low energy X-rays in the range of 8 keV (see Equation 2.1 and Figure 2.1).

$$\frac{I}{I_0} = \exp\left(-\sum_{i=1}^{k}\left(\frac{\mu_i}{\rho_i}\cdot\omega_i\right)\cdot d\cdot\rho\right) \qquad (2.1)$$

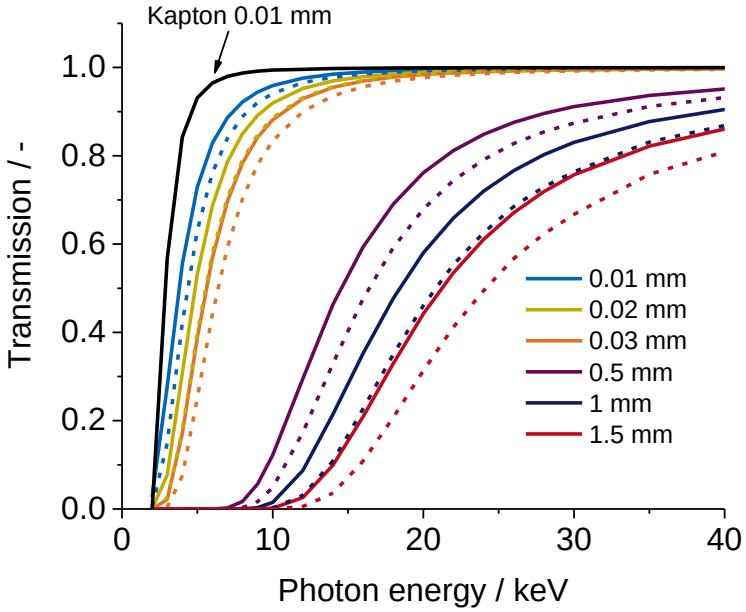

Figure 2.1: X-ray transmission of SiO_2 (solid line) and AlN (dotted lines) as a function of the incoming photon energy and the wall thickness.

Furthermore, reactors made from ceramic materials like AlN tend to have a high diffusion coefficient for gas molecules and therefore have to be sufficiently thick to prevent loss of e.g. hydrogen.

Polymers like Kapton exhibit good transmissibility for X-rays also in the low energy region (Figure 2.1) but have only minor temperature and pressure stability. Therefore, the material of choice for many studies is quartz glass with a wall thickness of 0.01 mm, which exhibits excellent X-ray transmissibility combined with high pressure and temperature stability. The maximum operating pressure of quartz capillaries can be calculated using equation 2.2.[13]

$$p = \frac{20 \cdot d_{wall} \cdot \frac{K}{s}}{d - d_{wall}} \qquad (2.2)$$

Depending on the wall thickness, capillaries with 1 mm outer diameter can withstand a pressure up to 50 bar and temperatures up to 1000°C (Figure 2.2).

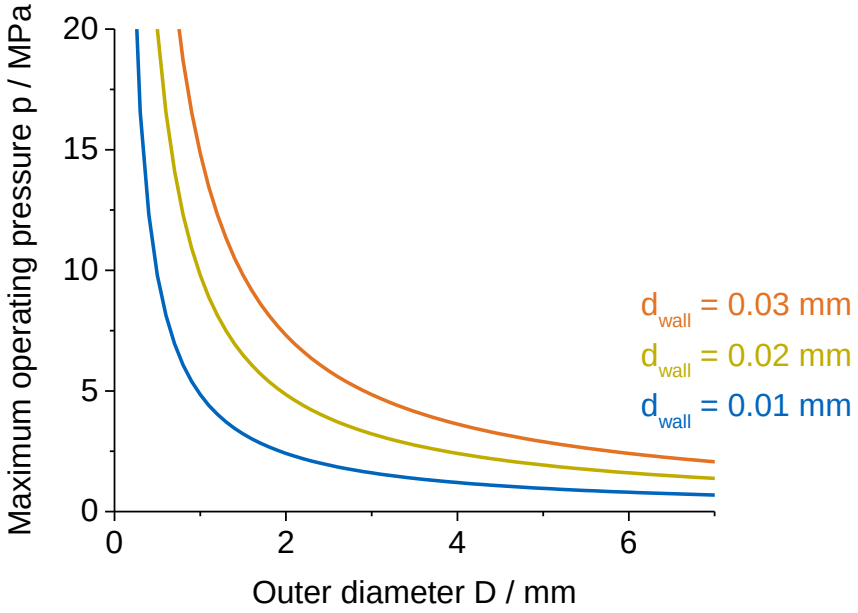

Figure 2.2: Maximum operating pressure of quartz capillaries considering a safety factor of s = 2 and a tensile strength of K = 48 MPa; wall thickness d_{wall} = 0.01 mm (blue line), d_{wall} = 0.02 mm (orange line) and d_{wall} = 0.03 mm (green line).

As new third-generation synchrotrons provide enough photon flux to reduce the time to obtain a spectrum with good signal to noise ratio from hours to minutes compared to first and second generation sources, the time necessary to pretreat a sample (e.g. activation) might be longer than the time needed to collect the spectra. Therefore, several approaches have been made to minimize the time for pretreatment via constructing parallel cells. Kimmerle et al.[14] arranged 6 capillaries in parallel in an oven that can reach temperatures up to 400°C and Bare et al.[5] designed a parallel reactor system which can reach 825°C at atmospheric pressure. Nevertheless, most of these systems suffer from some limitations in temperature (i.e. caused by the window material or by the glue to fix the capillaries) or in pressure due to the large diameter of the reactor.

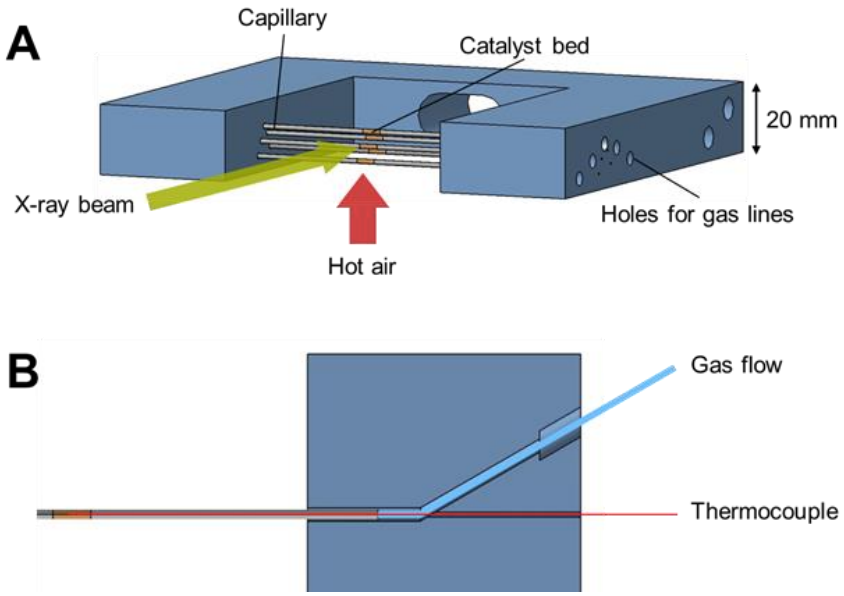

Figure 2.3: 3D model (A) of a fivefold capillary cell including connections for thermocouples and (B) visualization of the mounted capillary with gas connections and thermocouple.

Therefore, we developed a cell to overcome these limitations by designing a fivefold capillary cell allowing the pretreatment of up to 5 samples in parallel (Figure 2.3). Due to the usage of quartz capillaries with only 1 mm outer diameter and 10 µm wall thickness (WJM Glas, 100 mm length), the cell can be pressurized up to 50 bar. The capillaries can be loaded with ~4 mg of catalyst pressed and sieved to a fraction of 80 – 120 µm resulting in a catalyst bed length of 4 mm, which is fixed in the middle of the cell with quartz wool. This catalyst bed can be heated up to 1000°C from below with a hot air blower. As the hot air blower provides a radial heating zone of 8 mm in diameter, there is no temperature limitation due to the two component glue used to seal the capillaries in the U-shaped sample holder, as the distance between the heated zone and the resin is sufficiently large to avoid the thermal decomposition of the epoxy. For temperature monitoring, thermocouples can be placed in each capillary. The cell geometry can be used for measurements in transmission as well as in fluorescence mode and is very flexible with respect to pressure, as the wall thickness of the capillaries can be increased up to 30 µm. The advantage of this cell design is, that different gas mixtures and pressures can be applied to each capillary, while the temperature is the same in all five capillary reactors.

2.3.2 Gas distribution unit

To guarantee identical fluid dynamic conditions for every capillary and to ensure high flexibility with respect to feed gas composition, a gas distribution unit was designed which allows feeding individual gas mixtures to each capillary (Figure 2.4).

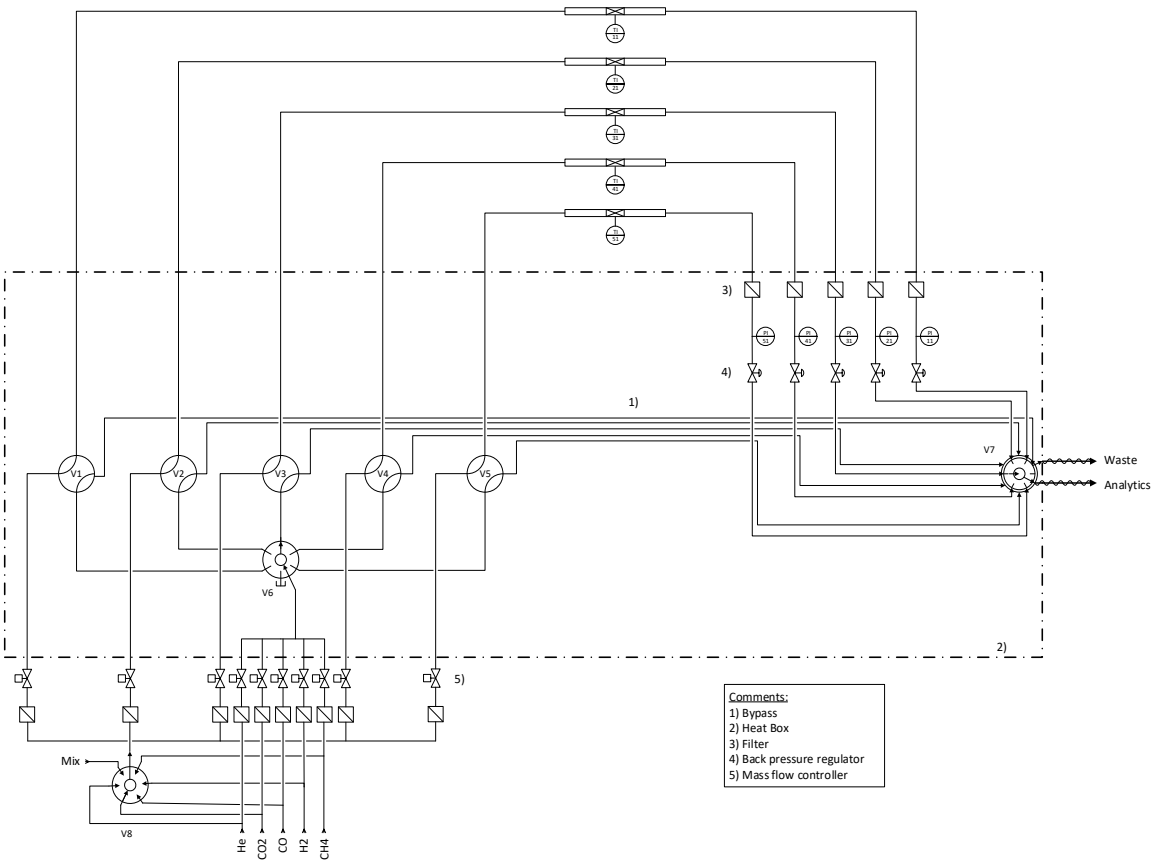

Figure 2.4: Flowsheet of the gas distribution unit designed for the fivefold capillary cell.

The advantage of this setup is that the pressure in each capillary can be controlled separately with a back pressure regulator. The setup contains several electronically controlled mass flow controllers to adjust the gas mixture for each capillary. Automatic valves are included to enable fast switches between the gas compositions. Furthermore, the gas distribution unit can be heated up to 200°C to prevent condensation of e.g. water. For safety reasons a gas monitoring system is connected to an automatic shut off which automatically switches of the gas flow in case of a leak.

2.3.3 Comparison of the signal quality

The novel capillary call was used to study several different catalysts, which are discussed in chapter 3 and 4. To give a general assessment on the usability of capillaries for X-ray absorption spectroscopy, the signal quality obtained with a capillary is compared to the signal quality from a conventional pellet cell as used in several studies.[15-21] For that purpose a Ni/ZrO_2 catalyst was prepared with a loading of 10 wt.% and measured directly after calcination. This type of catalyst is a good example for a sample, which is hard to measure in X-ray absorption spectroscopy, as the ZrO_2 support absorbs a large amount of photons. Figure 2.5 shows the comparison of the XANES before and after reduction in 10% H_2 at 600°C.

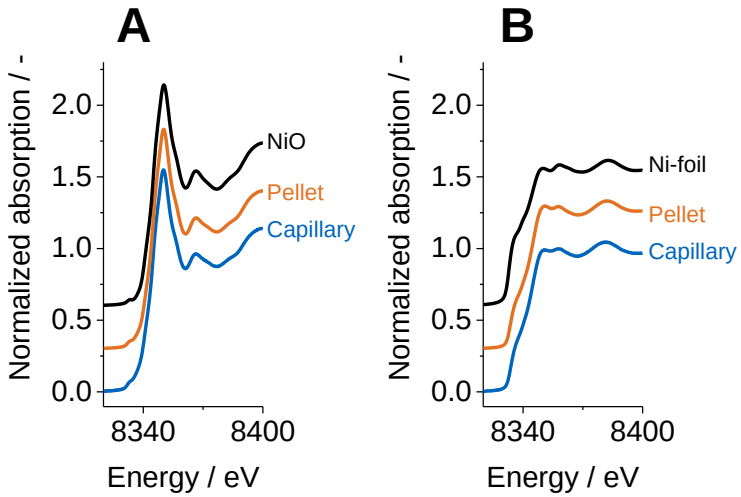

Figure 2.5: XANES of an oxidized (A) and a reduced (B) 10 wt.% Ni/ZrO_2 catalyst obtained with a pellet cell (orange line) and a capillary cell (inner diameter 0.98 mm, blue line) with Ni-foil and NiO as references (black line).

After calcination, the catalyst was fully oxidized as concluded from the position of the absorption edge. Comparing the shape of the white line with the XANES of NiO powder added as a reference again allows to conclude that Ni/ZrO_2 was fully oxidized after calcination. Please note that there is no difference with respect to signal quality observable in the XANES. Treating the catalyst in 10% H_2 in He leads to a decrease in white line intensity and to a shift of the absorption edge to 8333 eV. Comparing the shape of the white line and the position of the absorption edge with the XANES of a Ni foil allows to deduce that both samples were reduced to metallic Ni. Also in Figure 2.5 B no differences in signal quality can be observed. To further clarify if there is any difference in the signal quality of the spectra obtained in a pellet cell or in a capillary cell, EXAFS were analyzed and plotted in Figure 2.6.

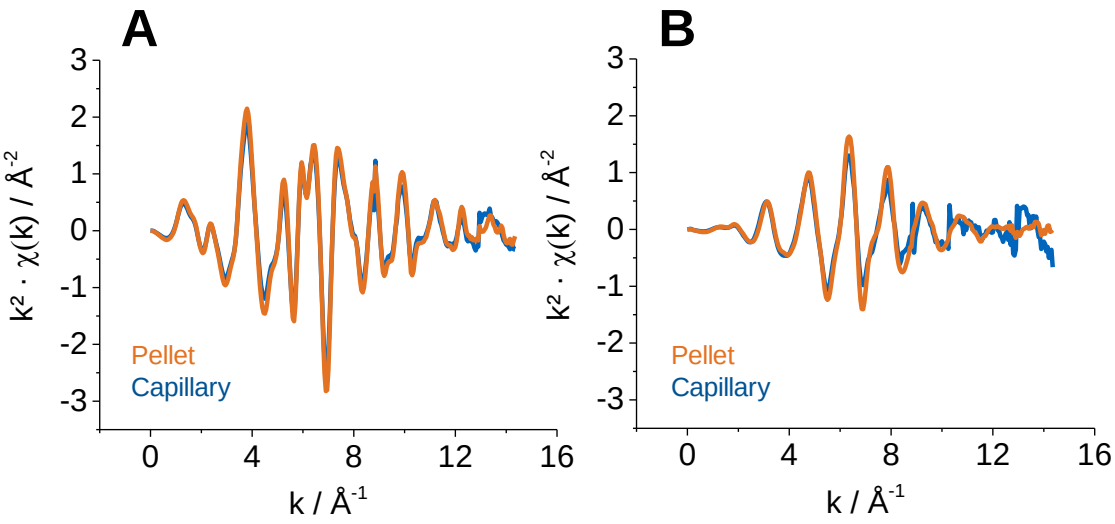

Figure 2.6: k^2-weighted χ(k) of an oxidized (A) and a reduced (B) 10 wt.% Ni/ZrO_2 catalyst obtained with a pellet cell (orange line) and with a capillary cell (inner diameter 0.98 mm, blue line).

For both, the oxidized and the reduced Ni/ZrO_2, the EXAFS obtained with the capillary cell and the pellet cell are identical up to k = 9 Å. For higher values of k, the signal in the capillary gets much noisier. This is caused by several effects. The sample in the pellet cell is very homogeneous, has equal thickness and is optimized for transmission experiments with respect to sample thickness and total absorption. As the capillary has a radial profile, the incoming photons at the margin have a lower absorption length compared to those in the middle of the capillary. Additionally, the catalyst in the capillary is pressed and sieved to a fraction of 80 – 120 µm, which also introduces noise to the signal.

2.3.4 Comparison of the kinetic data

Since operando studies have to be carried out under identical conditions as the kinetic experiments in lab-scale facilities, reactions in a capillary should show the same reaction rates and kinetic behavior compared to a lab scale reactor. Figure 2.7 shows the comparison of conversions obtained under almost equal space velocities for methane dry reforming at 800°C performed in a lab-scale reactor with 4 mm inner diameter and a capillary with 0.98 mm inner diameter.

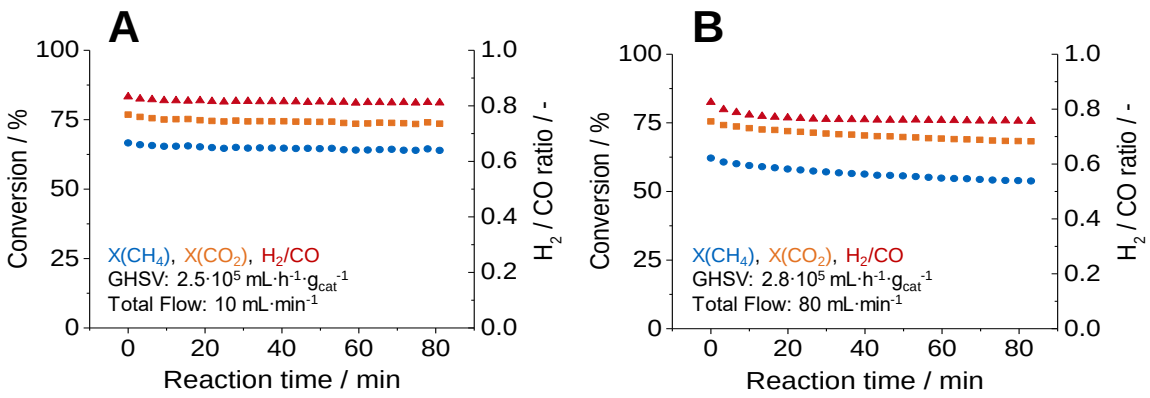

Figure 2.7: Comparison of kinetic data obtained with a Ni/ZrO_2 catalyst in a 1 mm capillary (A) and a 4 mm PFR (B); CH_4 conversion (blue dots), CO_2 conversion (orange squares) and H_2/CO ratio of the product gas (red triangles).

Both reactor types show almost equal conversion levels for CH_4 and CO_2 as well as similar H_2/CO ratios. The slightly lower conversion for the plug flow reactor is caused by the 10% higher space velocity. The difference between CH_4 and CO_2 conversion results from the contribution of the reverse water gas shift reaction (Equation 1.8) where CO_2 and H_2 is shifted to CO and H_2O. This leads to a higher CO_2 conversion and a lower H_2/CO ratio.

2.3.5 Structural changes of Ni particles during feed modulations

The above mentioned experiments were performed under stationary conditions, as a conventional EXAFS scan takes several minutes, depending on the sample quality and on the beamline layout. For this type of measurements, the residence time distribution of the cell is not that important, as monitoring of highly dynamic processes is not possible due to the low time resolution. As several chemical processes occur under fluctuating conditions (e.g. exhaust gas catalysis[22] or oxidation of CO[23]) new methods have been developed to drastically increase the time resolution to the range of milliseconds.[1] These measurements require cells with a PFR like residence time distribution allowing fast switches of the reactants. Capillary cells exactly meet those demands. To give an example of the usability of capillary cells, the structural changes of a Ni/ZrO_2 catalyst while changing the chemical potential from reducing (CH_4 + CO_2 in He) to oxidizing (CO_2) atmosphere has been followed by QEXAFS with a time resolution of 30 Hz at 800°C. Figure 2.8 A shows the time resolved XANES during feed modulations, whereas Figure 2.8 B shows the corresponding Fourier-transformed EXAFS.

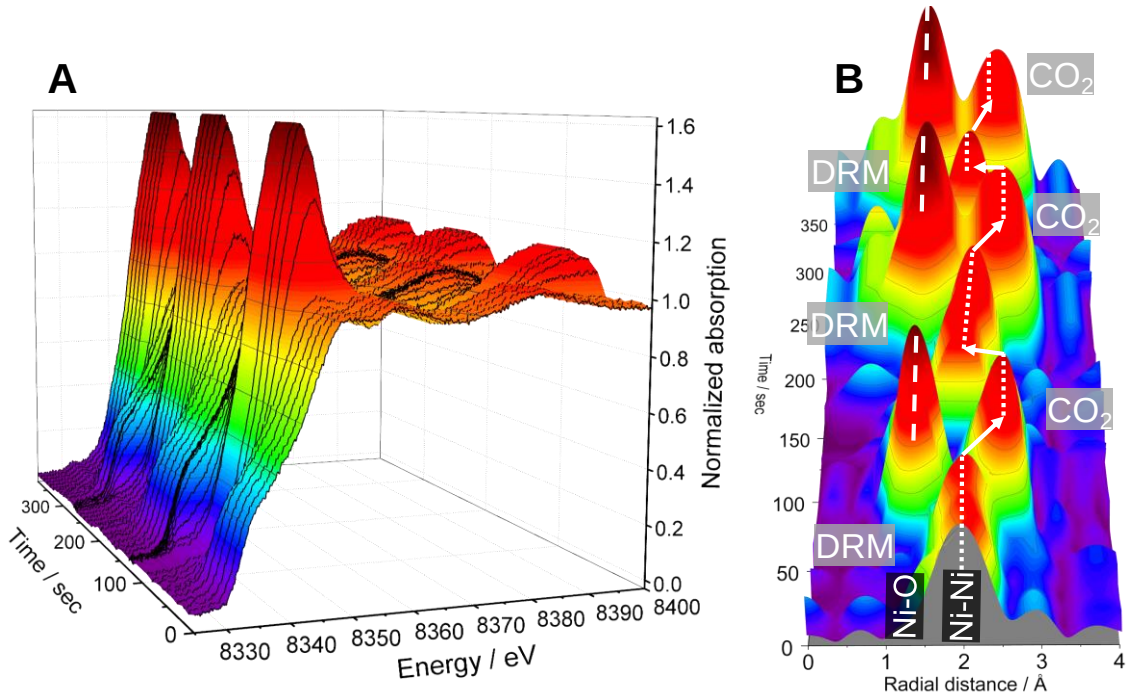

Figure 2.8: XANES recorded during periodic feed modulations from CH_4 + CO_2 in He to pure CO_2 over 10% Ni/ZrO_2 at 800°C followed by QEXAFS with a time resolution of 30 Hz (A) and Fourier-transformed EXAFS during the same process (B).

After the initial reduction at 600°C and the subsequent heating to 800°C the catalyst was fully reduced as concluded from the shape of the white line. During the first cycle of methane dry reforming (CH_4 + CO_2 in He) no changes in the oxidation state were observed. Switching from reforming atmosphere to CO_2 led to a slow increase in the intensity of the white line and to a shift of the absorption edge. Comparing the data with the XANES of NiO reveals a full oxidation of metallic Ni to NiO with CO_2 at 800°C. During the subsequent dry reforming cycle, NiO is rapidly reduced to metallic Ni again, as concluded from the white line intensity. During this reduction process, H_2 generated in the dry reforming reaction is consumed. The

structural response of the Ni particles during feed modulations can also be seen from the Fourier-transformed EXAFS signal in Figure 2.8 B. After the initial reduction only Ni-Ni contributions (dotted line in Figure 2.8 B) were present. Introducing CO_2 to the catalyst results in a slow expansion of the Ni-Ni distances and in the evolution of Ni-O contributions (dashed line in Figure 2.8 B) indicating an oxidation of the Ni particle. Reverting back to dry reforming atmosphere again results in a rapid contraction of the Ni-Ni distances and in the disappearance of Ni-O contributions pointing to a reduction of NiO to metallic Ni.

To get detailed information on the oxidation and reduction kinetics of a Ni particle, the novel fivefold capillary cell was packed with 5 capillaries, whereas each capillary was loaded with the same amount of catalyst. After fixing the capillaries in the sample holder, the capillaries were heated up to 800°C with 10 $K \cdot min^{-1}$ in pretreatment atmosphere to obtain pre-oxidized or pre-reduced Ni particles.

Table 2.1: Different treatment of five capillaries with the same amount of catalyst.

Capillary	Pretreatment	Reduction / oxidation agent
1	10% O_2 in He	10% H_2 in He
2	10% O_2 in He	10% CH_4 in He
3	10% O_2 in He	10% CH_4 + 10% CO_2 in He
4	10% H_2 in He	10% O_2 in He
5	10% H_2 in He	10% CO_2 in He

Table 2.1 summarizes the pretreatment of the capillaries. At 800°C, all catalysts were flushed with He before switching to the corresponding oxidizing / reducing agent. Please note that the usage of the fivefold cell ensured equal temperature for all capillaries and additionally decreased time for the pretreatment as this can be done in parallel for all samples. As the QEXAFS measurement cannot be done in parallel, the experiment started with switching the reactant gas for capillary 1 from He to 10% H_2 in He while recoding QEXAFS with a time resolution of 30 Hz. Linear combination analysis of the spectra with NiO and Ni-foil as references leads to the oxidation state of the Ni particles as a function of time (Figure 2.9 A and B), while fitting these data with a first order rate approach results in the first order rate constants (Figure 2.9 C). Please note the different time scales in Figure 2.9 A and B.

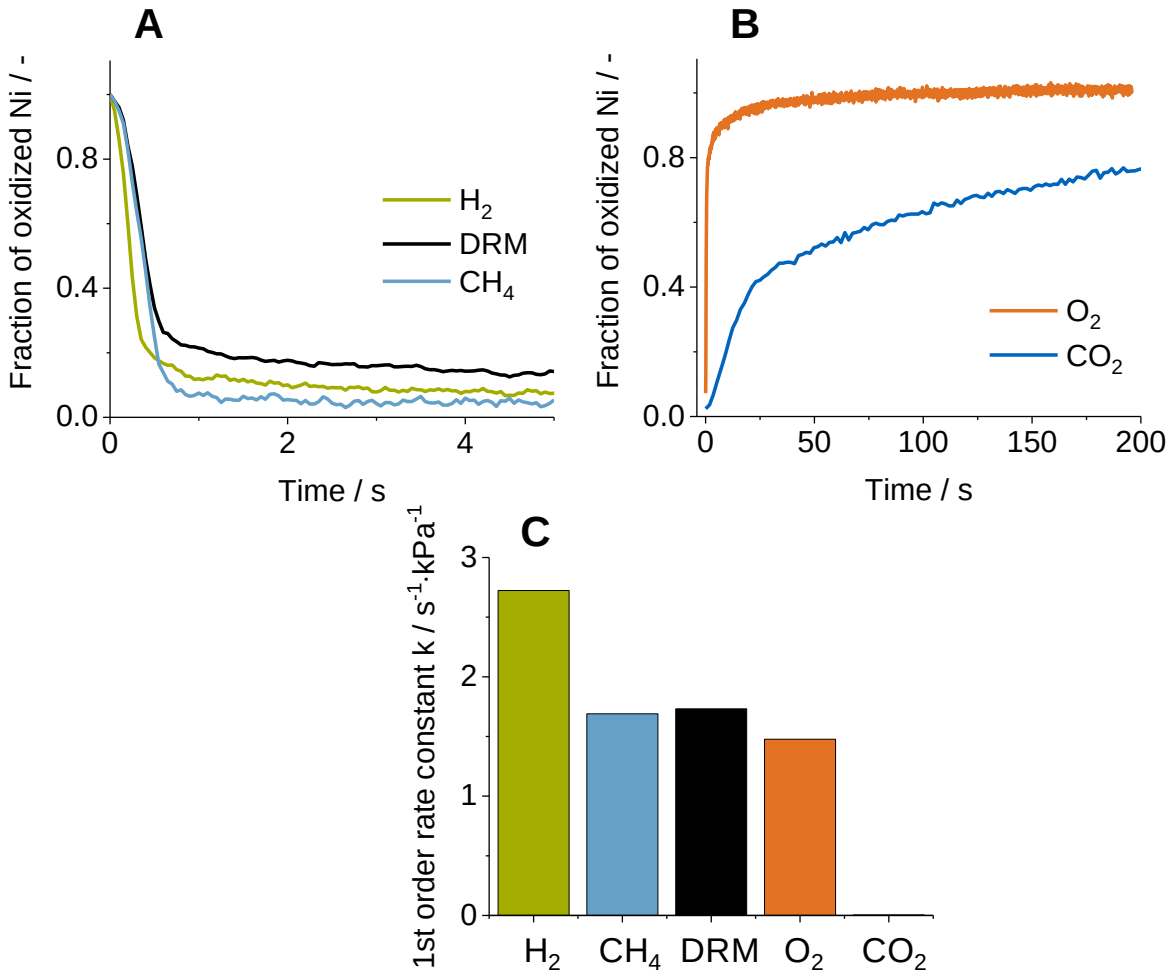

Figure 2.9: Variation of Ni^{2+} concentration (A and B) deduced by linear combination fitting of QEXAFS data while changing the chemical potential of the feed gas and analysis of the (1^{st} order) rate constant for the oxidation /reduction reaction (C).

Hydrogen reduces the Ni particles at the fastest rate, while the reduction with CH_4 and DRM reaction gas (10% CH_4 + 10% CO_2 in He) show almost the same rate constant of 1.7 s^{-1}·kPa^{-1}. The slower rate of reduction for CH_4 allows to conclude that CH_4 decomposition is the rate determining step in the oxidation of the Ni particles. It is conceivable that the reduction in presence of CH_4 and DRM reaction gas occurred at the same rate, as CH_4 decomposition is the rate determining step in methane dry reforming. The previously reduced samples were oxidized with 10% O_2 in He or 10% CO_2 in He, whereas the oxidation with O_2 occurs much faster compared to CO_2. Further investigation of oxidation mechanisms is presented in chapter 4.

In this type of experiments, the pretreatment takes much longer (1.5 h) compared to the measurement itself (several minutes for each capillary), which shows that the usage of a multi capillary system drastically reduces the beamtime necessary for these experiments. The novel cell combined with a highly flexible gas distribution unit enables efficient usage of highly time limited synchrotron radiation.

2.4 Conclusion

In the present study, we show the development of a novel fivefold capillary cell for in situ X-ray absorption spectroscopy as well as the advantages of capillary cells in contrast to conventional pellet cells. The advantage of quartz glass in contrast to kapton or ceramic materials is the broad operation window in temperature and pressure as well as the relatively low absorption for x-rays in the range of 8 keV. Furthermore, the PFR-like residence time distribution allows fast switches of the reactant gas composition which allows studies under transient conditions. The capillary cell developed in this study allows to study both, the structure and the activity of a catalyst sample in parallel, which serves as a basis for rational catalyst design.

For the two following chapters, the usage of the fivefold cell was essential to use the limited access to synchrotron radiation in an efficient way. Detailed analysis of the oxidation kinetics of a Ni particle with different oxidants is given in chapter 4, while in chapter 3 the role of the metal support interface in methane dry reforming is illustrated.

2.5 Associated Content

Publication

This chapter is based on a peer reviewed article (Matthias Steib, Andreas Jentys and Johannes A. Lercher; "Structural response of Ni/ZrO_2 to feed modulations during CH_4 reforming reactions." *Journal of Physics: Conference Series*. Vol. 712. No. 1. IOP Publishing, 2016.)

The content and structure of this chapter is different from the manuscript.

Contributions

Matthias Steib did main contributions in kinetic experiments, EXAFS measurements, data analysis and manuscript preparation. Andreas Jentys was the co-advisor and Johannes A. Lercher the principal investigator.

Acknowledgements

This work was financially supported by the BMBF under the project ZeitKatMat. The X-Ray absorption experiments were performed on the SuperXAS beamline at the Swiss Light Source, Paul Scherrer Institut, Villigen, Switzerland. The authors gratefully acknowledge the beamline scientist Maarten Nachtegaal for his help during the beamtime.

2.6 Literature

1. O. Muller, D. Lutzenkirchen-Hecht and R. Frahm, *Rev Sci Instrum*, 2015, **86**.
2. J. Lercher, J. Bitter, W. Hally, W. Niessen and K. Seshan, *Studies in Surface Science and Catalysis*, 1996, **101**, 463-472.
3. A. Bansode, G. Guilera, V. Cuartero, L. Simonelli, M. Avila and A. Urakawa, *Rev Sci Instrum*, 2014, **85**.
4. S. R. Bare, G. E. Mickelson, F. S. Modica, A. Z. Ringwelski and N. Yang, *Rev Sci Instrum*, 2006, **77**, 023105.
5. S. R. Bare and T. Ressler, *Advances in Catalysis, Vol 52*, 2009, **52**, 339-465.
6. S. R. Bare, N. Yang, S. D. Kelly, G. E. Mickelson and F. S. Modica, *Catal Today*, 2007, **126**, 18-26.
7. B. S. Clausen and H. Topsoe, *Catal Today*, 1991, **9**, 189-196.
8. S. D. M. Jacques, O. Leynaud, D. Strusevich, P. Stukas, P. Barnes, G. Sankar, M. Sheehy, M. G. O'Brien, A. Iglesias-Juez and A. M. Beale, *Catal Today*, 2009, **145**, 204-212.
9. R. E. Jentoft, S. E. Deutsch and B. C. Gates, *Rev Sci Instrum*, 1996, **67**, 2111-2112.
10. M. A. Newton, A. J. Dent, S. Diaz-Moreno, S. G. Fiddy, B. Jyoti and J. Evans, *Chem-Eur J*, 2006, **12**, 1975-1985.
11. M. A. Newton, S. G. Fiddy, G. Guilera, B. Jyoti and J. Evans, *Chem Commun*, 2005, DOI: 10.1039/b411493k, 118-120.
12. N. Tsapatsaris, A. M. Beesley, N. Weiher, H. Tatton, A. J. Dent, F. J. W. Mosselmans, M. Tromp, S. Russu, J. Evans, I. Harvey, S. Hayama and S. L. M. Schroeder, *X-Ray Absorption Fine Structure-XAFS13*, 2007, **882**, 597-599.
13. M. Dreher, E. De Boni, M. Nachtegaal, J. Wambach and F. Vogel, *Rev Sci Instrum*, 2012, **83**.
14. B. Kimmerle, P. Haider, J. D. Grunwaldt, A. Baiker, P. Boye and C. G. Schroer, *Appl Catal a-Gen*, 2009, **353**, 36-45.
15. S. Grundner, M. A. C. Markovits, G. Li, M. Tromp, E. A. Pidko, E. J. M. Hensen, A. Jentys, M. Sanchez-Sanchez and J. A. Lercher, *Nat Commun*, 2015, **6**.
16. S. Simson, A. Jentys and J. A. Lercher, *J Phys Chem C*, 2015, **119**, 2471-2482.
17. E. K. Hanrieder, A. Jentys and J. A. Lercher, *Catal Sci Technol*, 2016, **6**, 7203-7211.
18. E. K. Hanrieder, A. Jentys and J. A. Lercher, *J. Catal.*, 2016, **333**, 71-77.
19. J. Hein, O. Y. Gutierrez, S. Albersberger, J. Y. Han, A. Jentys and J. A. Lercher, *Chemcatchem*, 2017, **9**, 629-641.
20. J. Hein, O. Y. Gutierrez, E. Schachtl, P. H. Xu, N. D. Browning, A. Jentys and J. A. Lercher, *Chemcatchem*, 2015, **7**, 3692-3704.
21. J. Hein, A. Hrabar, A. Jentys, O. Y. Gutierrez and J. A. Lercher, *Chemcatchem*, 2014, **6**, 485-499.
22. A. Marberger, D. Ferri, M. Elsener and O. Krocher, *Angew Chem Int Edit*, 2016, **55**, 11989-11994.
23. V. Marchionni, M. Nachtegaal, A. Petrov, O. Krocher and D. Ferri, *16th International Conference on X-Ray Absorption Fine Structure (Xafs16)*, 2016, **712**.

3 Dynamic organization of Ni/ZrO_2 interfaces for methane dry reforming

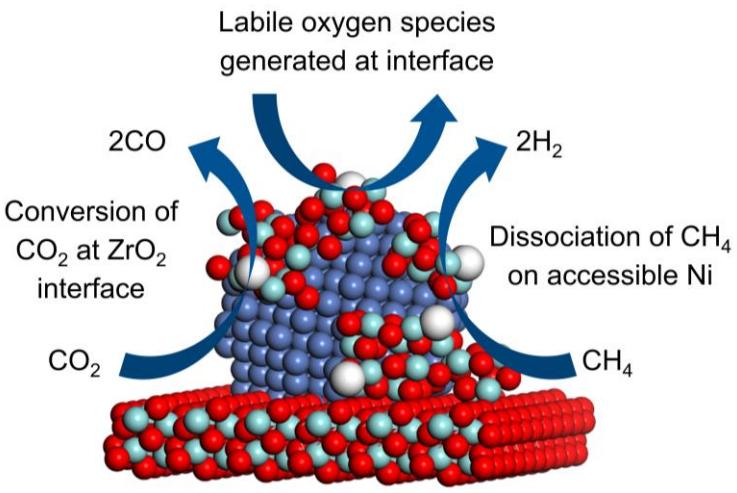

The activity of Ni/ZrO_2 catalysts for dry reforming of methane is significantly enhanced by activation and regeneration in presence of CO_2. The exposure to CO_2 maximizes and dynamically restructures the Ni-ZrO_2 interface leading to a higher availability of Ni surface sites. The ZrO_{2-x} at this interface acts catalytically by accepting and transferring one oxygen of CO_2 to the Ni surface, releasing CO in the decomposition of transiently formed carbonates. This opens a fast additional reaction pathway to convert CO_2, eclipsing the direct CO_2 dissociation on Ni. The kinetically controlled availability of atomic oxygen via this pathway reduces the carbon concentration on the surface, leading to less refractory carbon deposition and a more facile regeneration. The combination of a reducible support, which interacts moderately strong with Ni and a thermally less taxing regeneration with CO_2 leads to a general concept for stable operation of Ni based catalysts in dry reforming of methane.

3.1 Introduction

Dry reforming of methane, $CO_2 + CH_4 \leftrightharpoons 2\ CO + 2\ H_2$, leads to synthesis gas with H_2/CO ratios close to one and is frequently used to decrease this ratio in combined CH_4 reforming processes. To reach acceptable conversion levels, temperatures above 550°C are required.[1] While the activity is usually adjusted via the reaction temperature, stabilizing the catalyst against sintering and kinetically minimizing concentration of carbon deposits are critical challenges for an application on an industrial scale.[2] The large number of units installed to produce synthesis gas (worldwide 2378 units in operation in 2014, power equivalent of 117 GW thermal output)[3] require highly active, but also stable catalysts.[4] Noble and base metals can be used as catalytically active components, however, the large volume of the catalysts required for methane reforming allows only base metal catalysts such as Ni and Co to be economically feasible.[5]

For stabilizing the catalyst activity, the support plays an important role and its functionality at the metal support interface with respect to catalytic activity has been vividly debated.[6-11] Hypothesizing that CO_2 reduction may require a reducible oxide support Montoya et al. used a Ce doped ZrO_2 support to show oxygen mobility at the metal-support interface to be crucial for a stable catalyst.[12] Odedairo et al. reported that a plasma treatment of Ni/CeO_2 enhances the metal support interface and generates a clean metal surface, both effects leading to a higher activity in methane dry reforming.[7] Rezaei at al. have increased the metal support interface via synthesis of a high surface area CeO_2-ZrO_2.[9, 10] In contrast, Iglesia et al. concluded that the activity is only related to the type of the active metal and its particle size, leaving the reaction conditions to be most significant for catalyst stability [13] and proposed that the C-H bond breaking of CH_4 on the active metal is the rate determining step. Bitter et al. described a bifunctional mechanism for dry reforming of methane over Pt/ZrO_2 catalysts, where CH_4 is decomposed forming H* and CH_x* species on the metal surface, while CO_2 is predominantly adsorbed at the support forming carbonates.[14-16] Although great effort has been made in the development of a stable catalyst for methane dry reforming, carbon deposits might be formed, as the reacting gas composition in dry reforming favors carbon formation thermodynamically. These carbon deposits have to be removed periodically by oxidative treatments, which pose a challenge for catalyst stability in itself, as the oxidation of carbon deposits with O_2 is a highly exothermic reaction and the additional heat generation can induce catalyst deactivation due to sintering. Therefore, a thermally less demanding method to periodically remove carbon deposits has to be developed.

We report here a general concept for stable operation of Ni based catalysts for DRM, employing three approaches in parallel. We combine (i) a lower rate of coke formation by generating labile oxygen from CO_2 through CO_2 induced nano-restructuring of the Ni-ZrO_2 interface (ii) the stabilization of small metal domains at this interface via strong metal-support interactions, and (iii) the removal of deposited carbon via the thermally less taxing reverse Boudouard reaction compared to the conventional regeneration with O_2. The key to enable this concept is a reducible support that interacts moderately strong with CO_2, allowing transiently formed carbonates to dynamically adjust the Ni metal oxide interface and to generate sites which provide oxygen for the reforming process itself as well as for the

regeneration of the coked catalyst. We will show that exposing a Ni/ZrO_2 catalyst to CO_2 allows to maximize this interface and leads to a highly active catalyst. This will be combined with a periodic oxidative treatment in CO_2 for coke removal, which has no adverse influence on the activity of the catalyst compared to the regeneration in O_2. Combining steady state and transient kinetic measurements with X-ray absorption spectroscopy (XAS) the role of the individual steps for this new concept will be deduced.

3.2 Experimental

3.2.1 Catalyst preparation

Ni supported on SiO_2 (Evonik, Aerosil 200), Al_2O_3 (Evonik, Aeroxide AIUC) and ZrO_2 (Mel chemicals, XZO1501/03) was prepared by incipient wetness impregnation using an aqueous solution of nickel(II) nitrate hexahydrate (Acros, 99%) as described in detail previously.[17] After impregnation at room temperature, the catalysts were dried at 100°C for 12 h, calcined in air at 400°C for 2 h (flow rate: 100 mL·min^{-1}) and reduced with H_2 at 400°C (heating rate of 0.5 K·min^{-1}) for 2 h (flow rate: 100 mL·min^{-1}).

To follow structural changes of the Zr atoms in the support, a mixed SiO_2 – ZrO_2 network with 7 at.% of zirconia was impregnated via incipient wetness impregnation. The support was obtained via a base catalyzed condensation reaction according to Hahn et al..[18]

3.2.2 Activity measurements

The dry reforming reaction was carried out in a fixed-bed flow reactor at 800°C and atmospheric pressure. The catalysts were placed in a quartz reactor (4 mm diameter) and reduced in situ with H_2 for 1.5 h at 600°C. The reactant gases consisted of 15 vol.-% CH_4 (99.995 vol.%), 15 vol.-% CO_2 (99.995 vol.%) and 70 vol.-% He (99.999 vol.%) with a total flow of 50 mL·min^{-1}. The reaction products were analyzed online by mass spectrometry using a Pfeiffer Omnistar GSD 320.

3.2.3 Temperature programmed oxidation

Temperature programmed oxidation was carried out in a fixed-bed flow reactor after exposure to CO_2. The catalysts were placed in a quartz reactor (4 mm diameter). The reactant gases consisted of 10 vol.-% O_2 (99.995 vol.%), and 90 vol.-% He (99.999 vol.%) with a total flow of 50 mL·min^{-1}. The heating ramp was set to 5 K·min^{-1} witch a maximum temperature of 800°C. The reaction products were analyzed online by mass spectrometry using a Pfeiffer Omnistar GSD 320.

3.2.4 X-ray absorption spectroscopy

The X-ray absorption spectra were measured at the CLAESS beamline at the ALBA synchrotron in Barcelona, Spain. Data were recorded in fluorescence mode at the Ni K-edge at 8333 eV using a Si(111) crystal monochomator. QEXAFS data at the Ni-K edge were recorded the SuperXAS beamline at the SLS in Villigen, Switzerland using a channel-cut Si(111) monochromator with an oscillation frequency of 30 Hz.[19] The experiments at the Zr K-edge at 17998 eV were performed at the SuperXAS beamline at the SLS in Villigen, Switzerland recorded at the with a channel-cut Si(311) monochromator.[19]

All XAS experiments were carried out in situ in a quartz glass capillary (Hilgenberg, 1 mm diameter, 20 µm wall thickness). The flow of the reactant gasses during the experiment was

kept constant at 20 mL·min^{-1}. After flushing with He, the catalysts were heated up to 600°C (10 K·min^{-1}) in He and the reduction was performed in a mixture of 10% H_2 in He for 90 minutes. Subsequently the catalysts were heated to 800°C in He and the reaction was carried out using 15% CH_4 and 15% CO_2 in He. The regeneration was carried out in 100% CO_2 after flushing the capillaries with He. Data analysis was carried out with Athena and Artemis software from the IFEFFIT[20] package and with FEFF6.[21]

3.2.5 Infrared spectroscopy

IR spectra of adsorbed CO were measured on a Bruker Vertex 70 spectrometer at a resolution of 4 cm^{-1} collecting 128 scans in transmission absorption mode. The samples were pressed into self-supporting wafers and activated in flowing H_2 (p = 1 bar) for 1 h and in vacuum (p < 10^{-4} mbar) at 650°C for 0.5 h (heating rate of 10 K·min^{-1}).

IR spectra of adsorbed CO were measured after reduction in flowing H_2 (p = 1 bar) at 600°C for 1 h and outgassing for 1 h. CO was adsorbed at 40°C with p = 5 mbar followed by evacuation.

3.3 Results and discussion

The reaction rates for CH_4 conversion on Ni supported on SiO_2, Al_2O_3 and ZrO_2 at 800°C are shown as a function of time on stream in Figure 3.1.

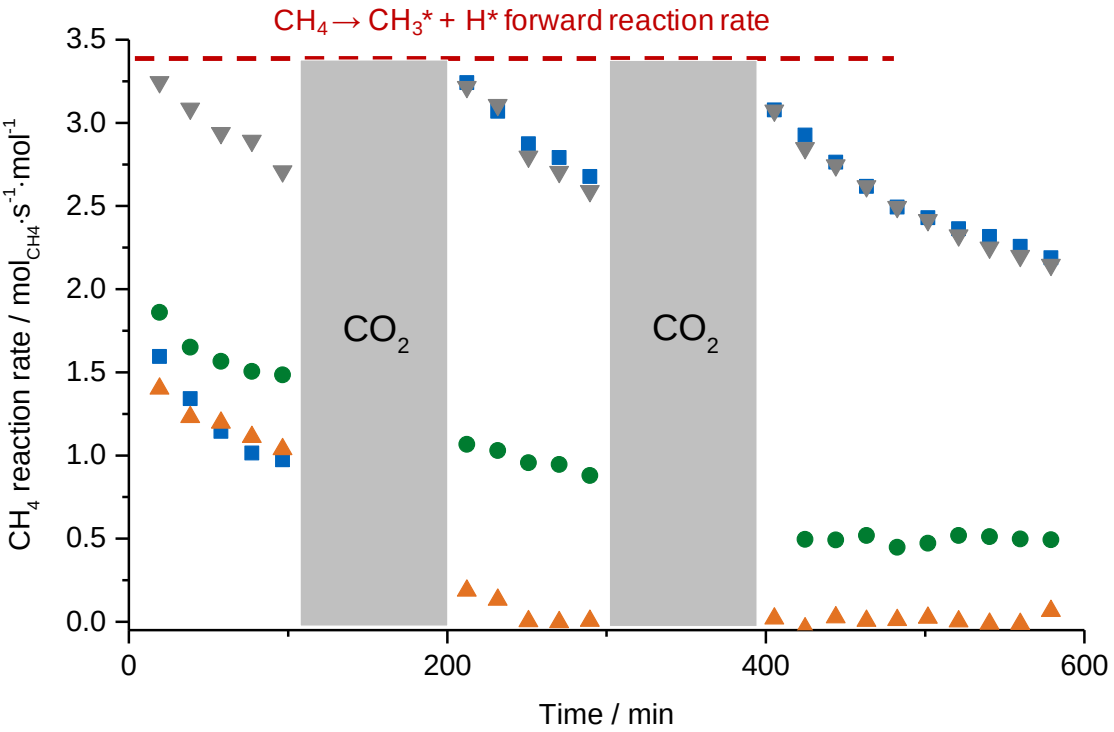

Figure 3.1: DRM rates for (■) Ni/ZrO_2, (●) Ni/Al_2O_3, (▲) Ni/SiO_2 and (▼) CO_2 treated Ni/ZrO_2 at 800°C before reaction. The catalysts were treated in 100% CO_2 in the sections indicated. The dashed red line designates the initial reaction rate for CH_4 decomposition at 800°C calculated from the data in reference [13].

In the first 90 minutes the rates on the three catalysts were decreasing with time on stream and were similar. At this point, the reaction was stopped and the catalysts were exposed to a stream of 100% CO_2 at 800°C for 90 minutes. After this step the rate on Ni/ZrO_2 increased markedly, approaching the initial reaction rate of CH_4 decomposition at 800°C (red line in Figure 3.1) calculated from the rates for dry reforming and CH_4 conversion reported in literature.[13] For Ni/Al_2O_3 the exposure to CO_2 did not affect the course of deactivation, while on Ni/SiO_2 almost no activity was observed in the second cycle of dry reforming. Two subsequent cycles with CO_2 exposure followed by DRM demonstrate that periodical reactivation of Ni/ZrO_2 with CO_2 restitutes the activity of Ni/ZrO_2. Temperature programmed oxidation of the catalysts after the exposure to CO_2 indicated that all carbon species were removed during the regeneration with CO_2 (Figure S3.1). It is interesting to note that treatment with CO_2 at 800°C before DRM increased the reaction rate to the level it reached otherwise after regeneration, which is somewhat less than a factor of three. Exposure to He at 800°C did not affect the activity.

In situ XAS at the Ni K-edge was used to monitor the oxidation state of Ni during the cycles of DRM and CO_2 treatment (Figure 3.2). During the first dry reforming cycle (after reduction in H_2 flow 10% H_2 in He, 1 bar, 600°C, 90 min) the shape of the white line (indicated by an arrow in Figure 3.2 A) and the pre-edge shoulder at 8330 eV in the XANES of Ni (Figure 3.2 A) showed that Ni/SiO_2 and Ni/ZrO_2 were fully reduced.

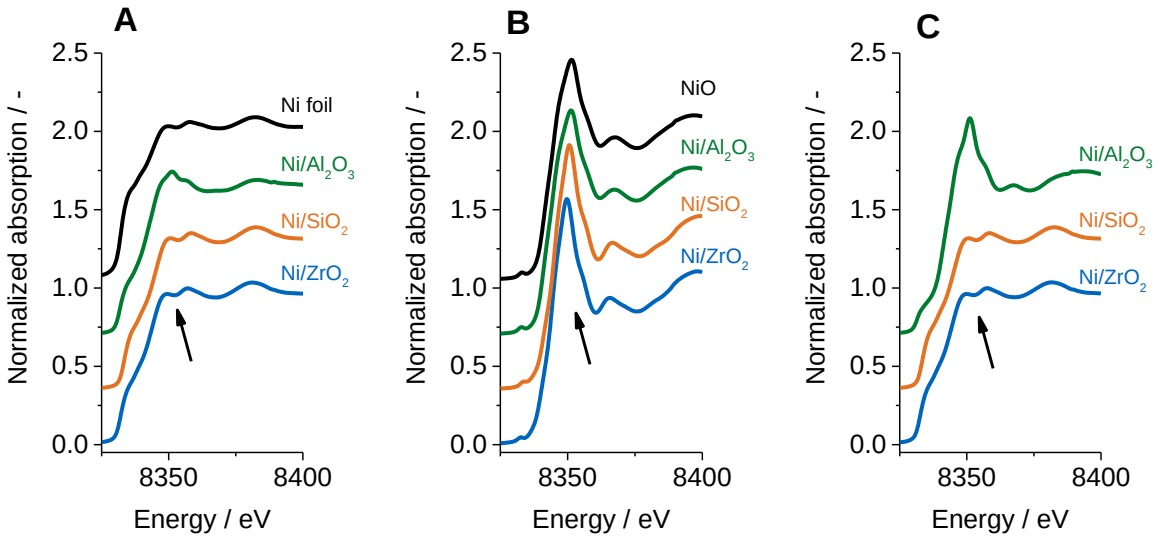

Figure 3.2: XANES recorded at the Ni K-edge of 5 wt.% Ni/ZrO_2 (blue), 5 wt.% Ni/SiO_2 (orange) and 5 wt.% Ni/Al_2O_3 (green) during the first DRM reaction cycle at 800°C (A), during the subsequent exposure to CO_2 at 800°C (B) and during the second DRM cycle at 800°C (C). XANES of Ni foil and bulk NiO are included for comparison (black).

The slightly higher white line for Ni/Al_2O_3 is attributed to a small fraction of oxidized Ni, present as Ni^{2+} in Ni aluminate.[22] After exposing the catalyst to CO_2 at 800°C, the intensity of the white line increased sharply for all catalysts. The comparison of the height and shape of the peak above the absorption edge with bulk NiO (black curve in Figure 3.2 B) indicates that Ni^0 was oxidized to Ni^{2+} in all catalysts. After reverting back to the DRM gas composition, Ni/SiO_2 and Ni/ZrO_2 were fully reduced, while Ni/Al_2O_3 remained oxidized. Al_2O_3 is known to form spinel structures such as $NiAl_2O_4$ with base metal oxides, which cannot be reduced under those conditions (Figure 3.2 C).[23]

It would be conceivable that the increase in the DRM rate after exposure to CO_2 is associated with the formation of smaller Ni particles formed during exposure to CO_2, as observed by Gonzalez during the exposure of a Ni/ZrO_2 catalyst to CO.[24] Therefore, the EXAFS before and after CO_2 treatment was measured to determine potential changes in the particle size (Figure S3.2 and Table S3.1-S3.4). The three catalysts showed only Ni-Ni contributions (R = 0.249 nm) and the particle size determined from the average coordination number calculated by assuming spherical particles was around 3 nm. After CO_2 exposure, the formation of NiO was observed from the appearance of Ni-O (R = 0.209 nm) and Ni-Ni (R = 0.295 nm) contributions for Ni/ZrO_2 Ni/SiO_2 and Ni/Al_2O_3. Ni/SiO_2 and Ni/ZrO_2 were reduced after changing back to the reactant gas, as concluded by the disappearance of the Ni-O contributions and the presence of short Ni-Ni distances. The Ni-Ni coordination number

for Ni/ZrO_2 was unaffected by the regeneration, which indicates that the particle size did not change during the oxidative regeneration in CO_2. For Ni/SiO_2 the coordination number increased from 10 to 11.5 after exposure to CO_2, which can be related to an increase in the metal particle size from 3 nm to 10 nm and to a decrease in the number of accessible surface Ni atoms by a factor of ~4, which fits to the significant decrease in activity. Ni/Al_2O_3 showed Ni-Ni contributions from reduced Ni (R = 0.249 nm) in the presence of the reactant gases, however, Ni atoms at larger Ni-Ni distances (R = 0.295 nm) and Ni-O contributions (R = 0.209 nm) were still observed resulting from the progressive formation of $NiAl_2O_4$. For Ni/SiO_2, the results show that sintering occurs predominantly under oxidative atmosphere as the interaction of NiO and support is low.[25] On Al_2O_3 we attribute the continued decrease in activity to the formation of stable $NiAl_2O_4$, which shows lower activity for dry reforming compared to metallic Ni.[23, 26] The difference in the average coordination numbers of Ni after regeneration over the three catalysts demonstrates that only ZrO_2 was able to efficiently stabilize the Ni particles during catalysis and regeneration.

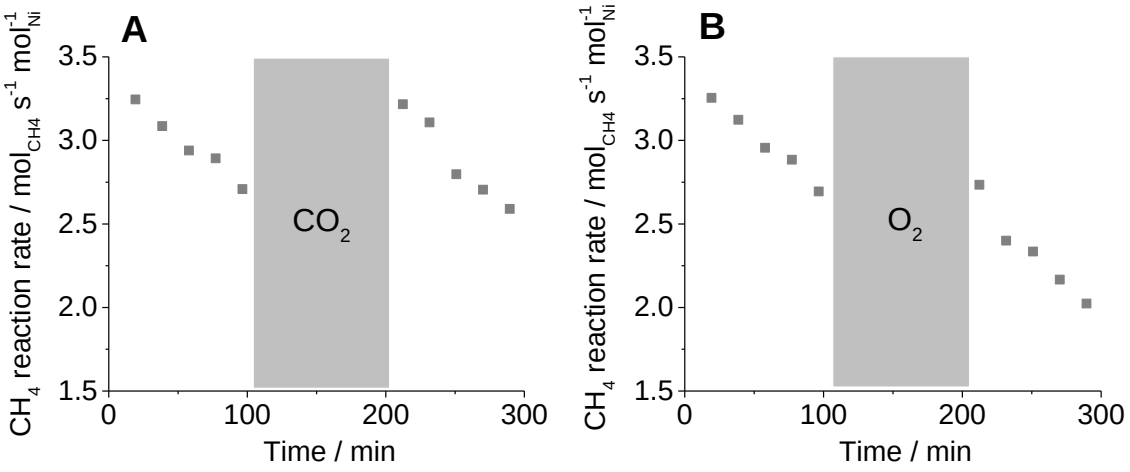

Figure 3.3: DRM rates over CO_2 treated Ni/ZrO_2. The catalysts were treated in situ at 800°C with 100% CO_2 (A) or 10% O_2 (B) in N_2 in the sections indicated.

The regeneration of the catalysts with CO_2 is compared to the typically applied reaction using O_2 as regeneration agent in Figure 3.3. These experiments showed that only CO_2 was able to fully restore the initial activity of Ni/ZrO_2. Please note that the formation of CO was observed when switching to CO_2 for regeneration, while the regeneration with O_2 led to the formation of CO_2. This indicates that the removal of carbon with CO_2 proceeds via the reverse Boudouard reaction. The analysis of the EXAFS (Table S3.5) indicated that the decrease in activity after coke removal with O_2 (Figure 3.3 B) is caused by sintering of metal particles due to the strongly exothermic oxidation reaction. (Table 3.1). In contrast, the removal of carbon deposits via the reverse Boudouard reaction as well as the oxidation of the metal particles with CO_2 is endothermic.

Table 3.1: Reaction equations and corresponding reaction enthalpies for different oxidation reactions of Ni and carbon.

1.	$CO_2 + C \rightleftharpoons 2CO$	$\Delta H^0 = +172\ kJ \cdot mol^{-1}$
2.	$Ni + CO_2 \rightleftharpoons NiO + CO$	$\Delta H^0 = +47\ kJ \cdot mol^{-1}$
3.	$C + O_2 \rightleftharpoons CO_2$	$\Delta H^0 = -395\ kJ \cdot mol^{-1}$
4.	$2Ni + O_2 \rightleftharpoons 2NiO$	$\Delta H^0 = -235\ kJ \cdot mol^{-1}$

In order to characterize the interaction of CO_2 with ZrO_2, XANES of highly dispersed ZrO_2 on SiO_2 were measured. This high dilution was required to monitor changes in the local environment of the Zr atoms during CO_2 exposure, as for conventional Ni/ZrO_2 catalyst the large number of Zr atoms in the bulk would not allow to identify subtle changes in its chemical state. XANES were recorded at the Zr-K edge in He at 800°C (after reduction at 600°C), during the first reaction cycle, the first CO_2 cycle and during the second reaction cycle (Figure 3.4).

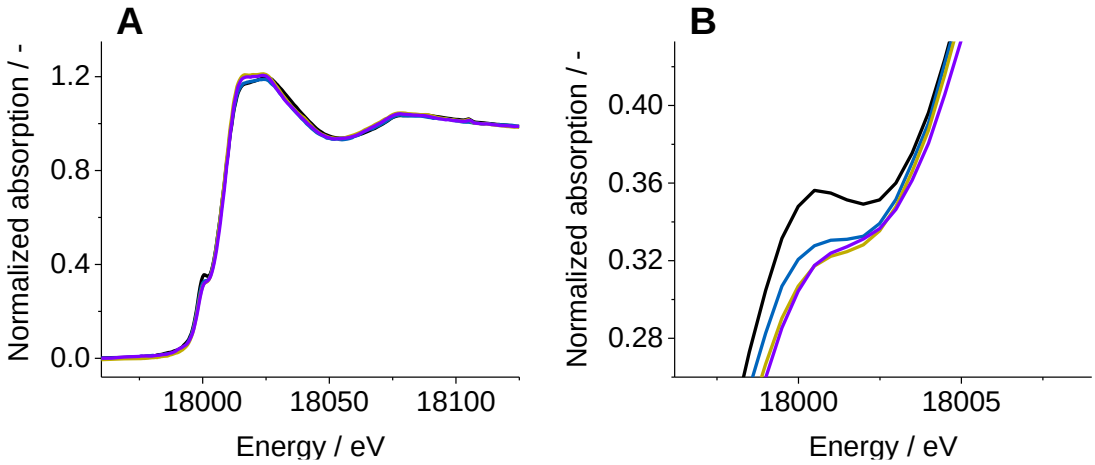

Figure 3.4: XANES at the Zr K-edge recorded at 800°C of a 5 wt.% Ni/ZrO_2 - SiO_2 after reduction at 600°C in 10% H_2 in He (black), during the first DRM reaction cycle at 800°C (blue), the subsequent exposure to CO_2 (purple) and the second DRM reaction cycle (yellow). (A) XANES at the Zr K-edge and (B) magnification of the region assigned to the 1s – 4d transition.

Two peaks were observed in the XANES at the Zr K-edge in the region from 18015 – 18035 eV (Figure 3.4 A), which are characteristic for differences in the Zr environment.[27-29] After the initial reduction, both peaks were lower compared to the subsequent reaction cycle. This indicates a partial oxidation of Zr under dry reforming conditions. To get deeper insight into the local environment of the Zr, the pre-edge at 18000 eV was analyzed. After the initial reduction at 600°C the highest intensity of the pre-edge peak at 18000 eV (Figure 3.4 B) was observed. This absorbance is assigned to the 1s-4d transition,[27] which is forbidden in a centrosymmetric environment.[30] Thus, the appearance of this peak indicates changes in the Zr-O tetrahedral in the tetragonal ZrO_2 as depicted in Figure 3.5.

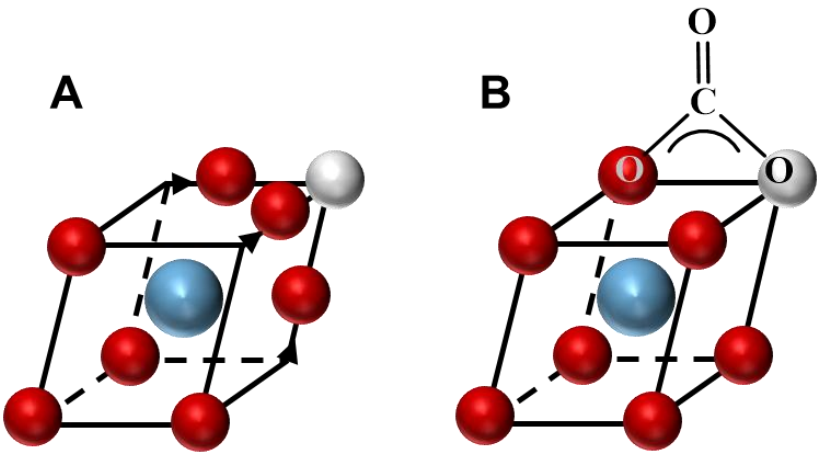

Figure 3.5: Schematic model of a distorted tetragonal ZrO_2 lattice with an oxygen vacancy (A) and a tetragonal ZrO_2 lattice with a filled oxygen vacancy (B). Red spheres represent oxygen anions, blue spheres Zr cations and grey spheres represent oxygen vacancies.

Initial reduction led to the removal of oxygen atoms from the ZrO_2 lattice in proximity to the Ni particle. The distortion of the local environment of Zr results from the formation of an oxygen vacancy (Figure 3.5 A) and caused the intense pre-edge peak at 18000 eV. The enhanced Lewis acidity generated by the local defect at the metal support interface has been shown to be crucial to activate CO_2.[31] In reaction atmosphere the vacancies are saturated with oxygen from CO_2, which restored the centrosymmetry and led to the decrease in the intensity of the pre-edge peak as depicted in Figure 3.5 B. This indicates that under steady state reaction conditions the presence of CO_2 increased the pool of labile oxygen species i.e., oxygen that is readily removed in reductive atmosphere, thus, enhancing the available oxygen that can be spilled over to Ni.[13, 14]

In order to analyze the role of the support on the kinetics of the oxidation, QEXAFS with a time resolution of 30 Hz were recorded during switching from He to CO_2 over Ni/SiO_2 and Ni/ZrO_2 before and after regeneration in CO_2 (Figure 3.6 A). The oxidation rate of Ni by CO_2 strongly depended on the support (Figure 3.6 B, orange and blue bar). The oxidation of Ni/ZrO_2 with CO_2 was significantly faster compared to the oxidation of Ni on SiO_2. It should be emphasized that CO was the only product formed after exposing both catalysts to CO_2 (Figure S3.3).

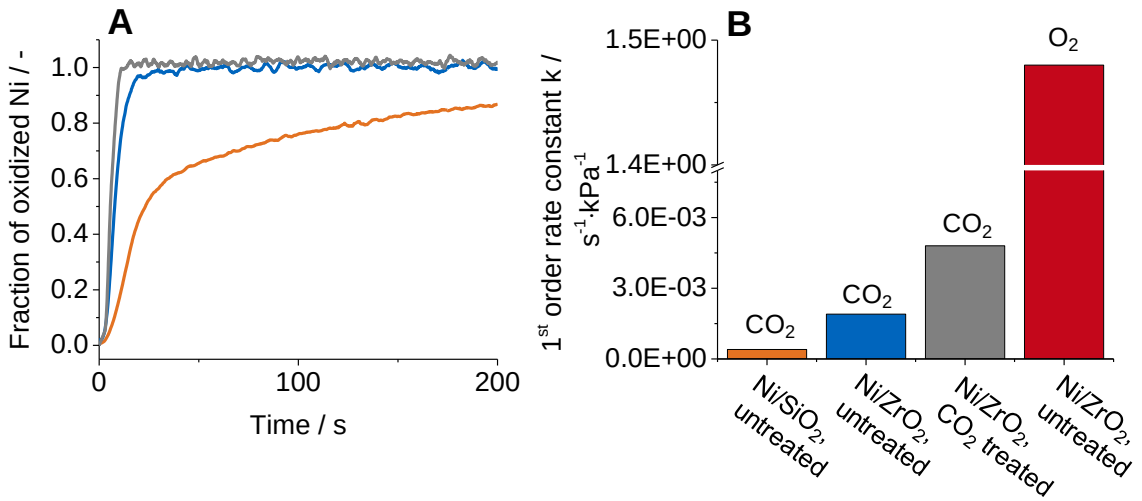

Figure 3.6: Variation of Ni^{2+} concentration (A) deduced by linear combination fitting of QEXAFS data while switching from He to CO_2 and analysis of the (1st order) rate constant for the oxidation reaction (B): Ni/SiO_2 (orange), Ni/ZrO_2 after reduction (blue), Ni/ZrO_2 after CO_2 treatment (grey) and Ni/ZrO_2 oxidized with O_2 (red).

The first order rate constants of the oxidation reaction are compared in Figure 3.6 B. As the rate of oxygen formation from CO_2 dissociation and the subsequent oxidation of the metal particles should not differ between Ni/SiO_2 ($k = 0.0004\ s^{-1}\cdot kPa^{-1}$) and Ni/ZrO_2 ($k = 0.0019\ s^{-1}\cdot kPa^{-1}$) for particles with the same size, differences in the oxidation rate indicate the existence of a second pathway for CO_2 activation presumably at the metal support interface of ZrO_2.[32, 33] Repeated exposure of Ni/ZrO_2 to CO_2 with intermittent reduction led to a further enhancement of the rate of oxidation of Ni by a factor of 2.5 ($k = 0.0048\ s^{-1}\cdot kPa^{-1}$, grey dataset in Figure 3.6), which points to an increase in the availability of sites at the interface between Ni and ZrO_2. The higher oxidation rate of Ni/ZrO_2 with O_2 compared to the oxidation with CO_2 (Figure 3.6 B, red and blue bar) shows that the rate of oxidation depends also on the oxidant. This indicates that regeneration of coked catalysts with CO_2 via the endothermic reverse Boudouard reaction is advantageous over the use of O_2.

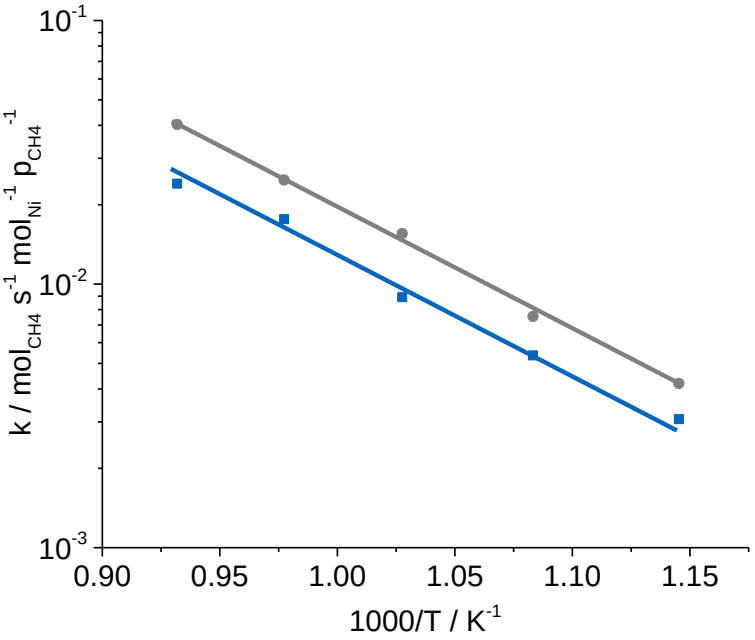

Figure 3.7: Arrhenius plot for dry reforming over CO_2 (●) treated and (●) untreated Ni/ZrO_2.

The apparent activation energies for the DRM reaction before and after regeneration in CO_2 (87 +/- 2 kJ·mol^{-1}) are compared in Figure 3.7. The identical values observed across the entire temperature range studied indicate that the reaction mechanism in not affected by the regeneration in CO_2.[2] It has been paradigmatically stated in literature e.g.[13, 34] that C-H activation is rate determining for DRM. Thus the increase of the pre-exponential factor by 2.5 times indicates a higher concentration of metal sites available for CH_4 conversion after exposure to CO_2. It has to be noted that the increase in CH_4 turnover rate by regeneration and the increase of the rate of oxidation of Ni were fortuitously equal (i.e., both increased approximately 2.5 times). In order to independently determine the concentration of the sites on the metal particles and at the metal support interface, IR spectra of adsorbed CO were measured (Figure 3.8 and Table 3.2). The bands of adsorbed CO above 2000 cm^{-1} are typical for linearly bonded CO on Ni.[35] The shoulder observed above 2100 cm^{-1} is attributed to CO adsorbed on partially oxidized Ni.[35, 36] In accordance to Goodman et al., we assign the band at 2085 cm^{-1} to CO adsorbed on Ni at the metal support interface.[37] Note that this allows to differentiate the sites on the metal surface (bands below 2075 cm^{-1}) and Ni sites in vicinity of the ZrO_2 support (band at 2085 cm^{-1}).

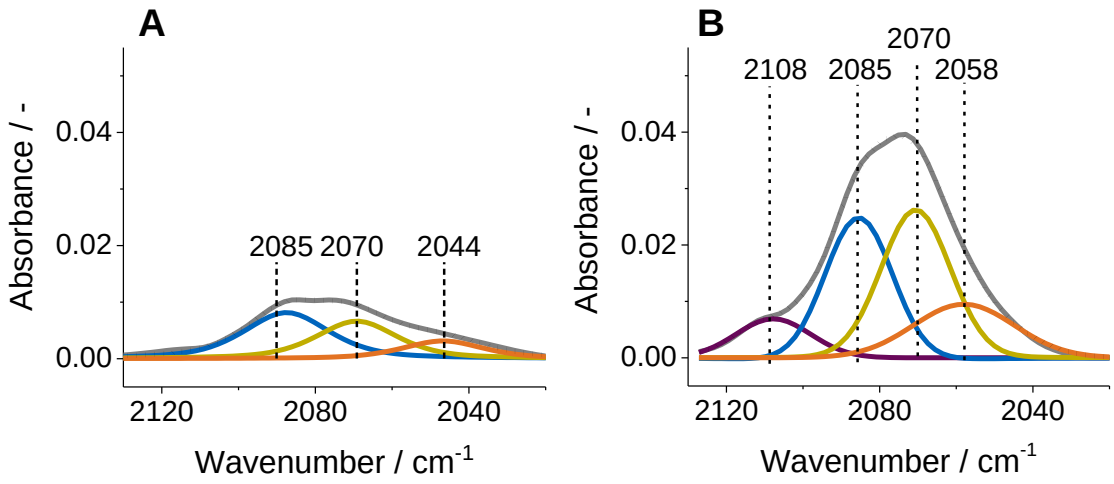

Figure 3.8: IR spectra of CO adsorbed at 5 mbar followed by evacuation on the untreated (A) and CO_2 treated (B) Ni/ZrO_2 catalyst.

After CO_2 exposure, the intensity of the sum of the bands attributed to Ni surface sites increased 2.9 times (pointing to a three-fold higher concentration of accessible Ni, when assuming an identical adsorption coefficient of CO on Ni), while the band at 2085 cm^{-1} increased nearly by a factor of 2, which is in good agreement with the increase in rate of CH_4 activation during DRM.

Table 3.2: Intensities of IR bands after CO adsorption.

Before CO_2 treatment		After CO_2 treatment	
Position / cm^{-1}	Area	Position / cm^{-1}	Area
		2108	0.168
2085	0.282	2085	0.516
2070	0.217	2070	0.603
2044	0.103	2058	0.313
∑	0.602	∑	1.600

3.4 Conclusion

Exposure of Ni/ZrO_2 to CO_2 at high temperatures increases the activity of the catalysts for DRM as well as the rate of oxidation of the Ni particles. The concentration of sites at the interface between the support and the metal is enhanced, leading to coordinatively unsaturated zirconia at the interface, which is able to transiently form carbonates and dissociate these into CO and the labile oxygen that can migrate across the metal particle.

The proposed reaction mechanism is illustrated in Figure 3.9. The increase in rate is attributed to a higher concentration of accessible Ni metal sites (preventing covering of the metal by ZrO_2 suboxides). The stability is enhanced by the presence of labile atomic oxygen,

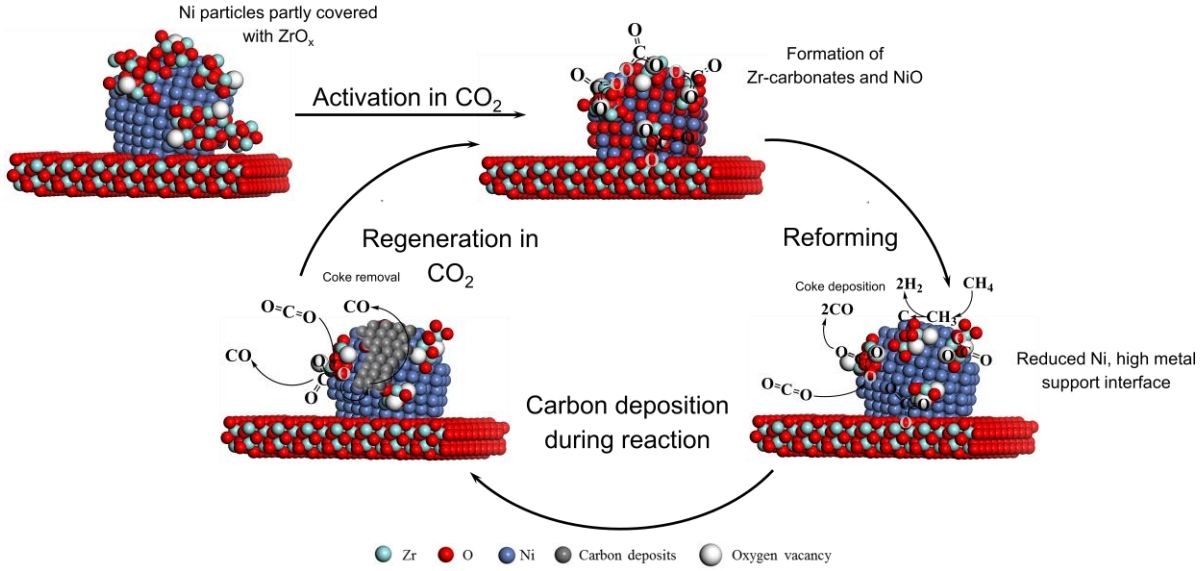

Figure 3.9: Schematic representation of the elementary steps of CO_2 treatment.

which readily oxidizes surface carbon formed during the dissociation of methane. The generation of this labile oxygen through transiently formed carbonates at the metal support interface increases in parallel the fraction of accessible Ni surface sites. In DRM, this effect causes the approximately three-fold higher reaction rate by providing additional oxygen to remove carbon formed by the rate determining CH_4 dissociation. During regeneration, the availability of oxygen via this route leads to the formation of CO via the (endothermic) Boudouard reaction, which is not as taxing with respect to heat evolution than the more conventional (exothermic) regeneration with O_2. While the nature of the ZrO_2 species at the Ni particles cannot be deduced from the current experiments, all observations are consistent with the fact that treatment with CO_2 maximizes the accessible ZrO_2 - Ni boundary as well as the concentration of metal surface sites. Overall, the results show that (inexpensive) Ni can be successfully used as catalyst in methane dry reforming, when ZrO_2 is used as support, generating a highly dynamic catalyst, which restructures itself during catalysis and regeneration by CO_2 on a nanoscopic level.

3.5 Associated Content

Publication

This chapter is based on an article with the same title submitted to ChemCatChem.
The structure and content of this chapter is different to the manuscript.

Contributions

Matthias Steib did main contributions in kinetic experiments, EXAFS measurements, data analysis and manuscript preparation. Yu Lou contributed with respect to IR spectroscopy, kinetic experiments and manuscript preparation. Andreas Jentys was the co-advisor and Johannes A. Lercher the principal investigator.

Acknowledgements

This work was financially supported by the European Union under project ERA Chem and the BMBF under the project ZeitKatMat. The X-Ray absorption experiments were performed on the SuperXAS beamline at the Swiss Light Source, Paul Scherrer Institut, Villigen, Switzerland and at the CLAESS beamline at ALBA Synchrotron with the collaboration of ALBA staff. The authors gratefully acknowledge the beamline scientists Maarten Nachtegaal and Laura Simonelli for their help during the beamtime.

3.6 Appendix

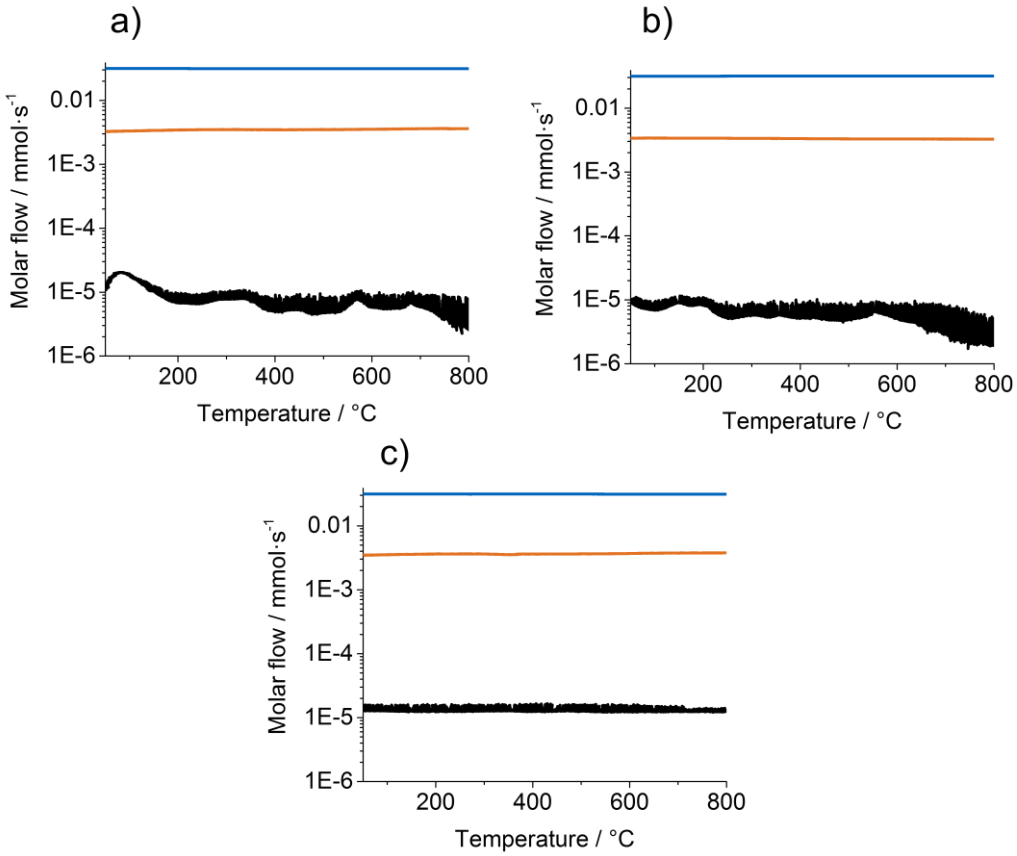

Figure S3.1: CO_2 (black line), O_2 (orange line) and He (blue line) signal during temperature programmed oxidation of Ni/ZrO_2 (a), Ni/SiO_2 (b) and Ni/Al_2O_3 (c) after one reaction cycle followed by CO_2 exposure.

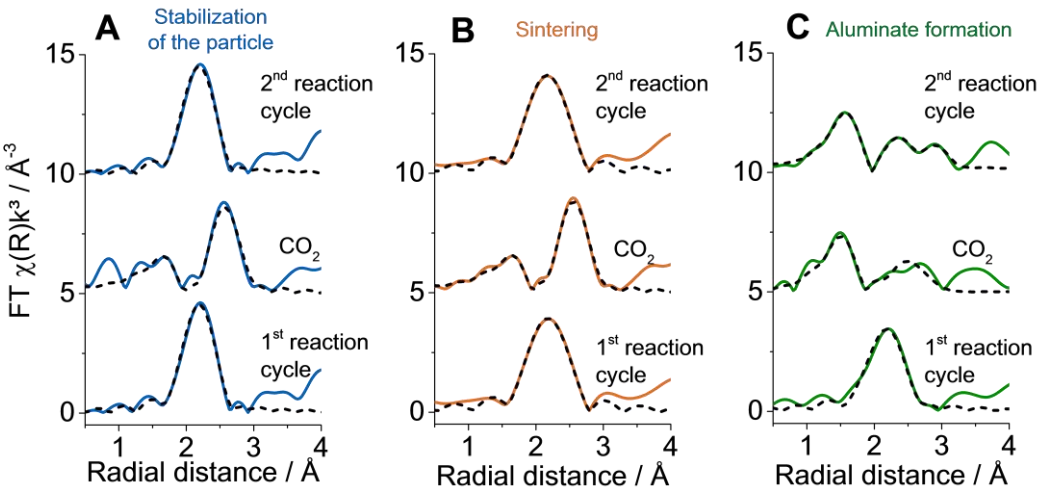

Figure S3.2: Fourier-transformed EXAFS at the Ni K-edge recorded at room temperature (A) 5 wt.% Ni/ZrO_2, (B) 5 wt.% Ni/SiO_2 and (C) 5 wt.% Ni/Al_2O_3 after the first reaction cycle, subsequent exposure to CO_2 and the second reaction cycle.

Table S3.1: Coordination numbers of Ni on the different catalysts after DRM reaction and activation in CO_2

	Ni/ZrO_2			**Ni/SiO_2**			**Ni/Al_2O_3**		
	Ni-Ni (Ni)	Ni-Ni (NiO)	Ni-O (NiO)	Ni-Ni (Ni)	Ni-Ni (NiO)	Ni-O (NiO)	Ni-Ni (Ni)	Ni-Ni (NiO)	Ni-O (NiO)
After 2nd reaction	10.0			11.5			8.4	11.4	5.9
After 1st CO_2		10.1	5.1		11.5	5.8		11.2	5.0
After 1st reaction	10.0			10.7			11.0		

Table S3.2: Fit results of a 5% Ni/ZrO_2 catalyst during cycle experiments.

Ni/ZrO_2	Ni-Ni				Ni-O			
	N	ΔE_0 [eV]	R [Å]	σ^2 [Å²]	N	ΔE_0 [eV]	R [Å]	σ^2 [Å²]
After 2nd reaction	10.0	7.1	2.493	0.006				
After 1st CO_2	10.1	3.7	2.948	0.006	5.0	0.5	2.091	0.05
After 1st reaction	10.0	7.7	2.490	0.005				

Table S3.3: Fit results of a 5% Ni/SiO_2 catalyst during cycle experiments.

Ni/SiO_2	Ni-Ni				Ni-O			
	N	ΔE_0 [eV]	R [Å]	σ^2 [Å²]	N	ΔE_0 [eV]	R [Å]	σ^2 [Å²]
After 2nd reaction	11.5	6.6	2.481	0.006				
After 1st CO_2	11.5	4.3	2.945	0.005	5.8	1.1	2.090	0.006
After 1st reaction	10.7	7.4	2.488	0.006				

Table S3.4: Fit results of a 5% Ni/Al_2O_3 catalyst during cycle experiments.

Ni/Al_2O_3	Ni-Ni (Ni)				Ni-Ni (NiO)				Ni-O			
	N	ΔE_0 [eV]	R [Å]	σ^2 [Å²]	N	ΔE_0 [eV]	R [Å]	σ^2 [Å²]	N	ΔE_0 [eV]	R [Å]	σ^2 [Å²]
After 2nd reaction	8.4	8.0	2.489	0.006	11.4	3.8	2.948	0.01	5.9	6.4	2.084	0.006
After 1st CO_2					11.2	4.0	2.948	0.002	5.0	5	2.084	0.003
After 1st reaction	11.0	6.9	2.489	0.007								

Table S3.5: Fit results of a 5% Ni/ZrO_2 catalyst during exposure to O_2 instead of CO_2.

Ni/ZrO_2	Ni-Ni				Ni-O			
	N	ΔE_0 [eV]	r [Å]	σ^2 [Å²]	N	ΔE_0 [eV]	r [Å]	σ^2 [Å²]
After 2nd reaction	11.1	7.2	2.488	0.005				
After O_2	10.6	4.8	2.942	0.006	5.3	1.0	2.093	0.005
After 1st reaction	10.0	7.7	2.490	0.005				

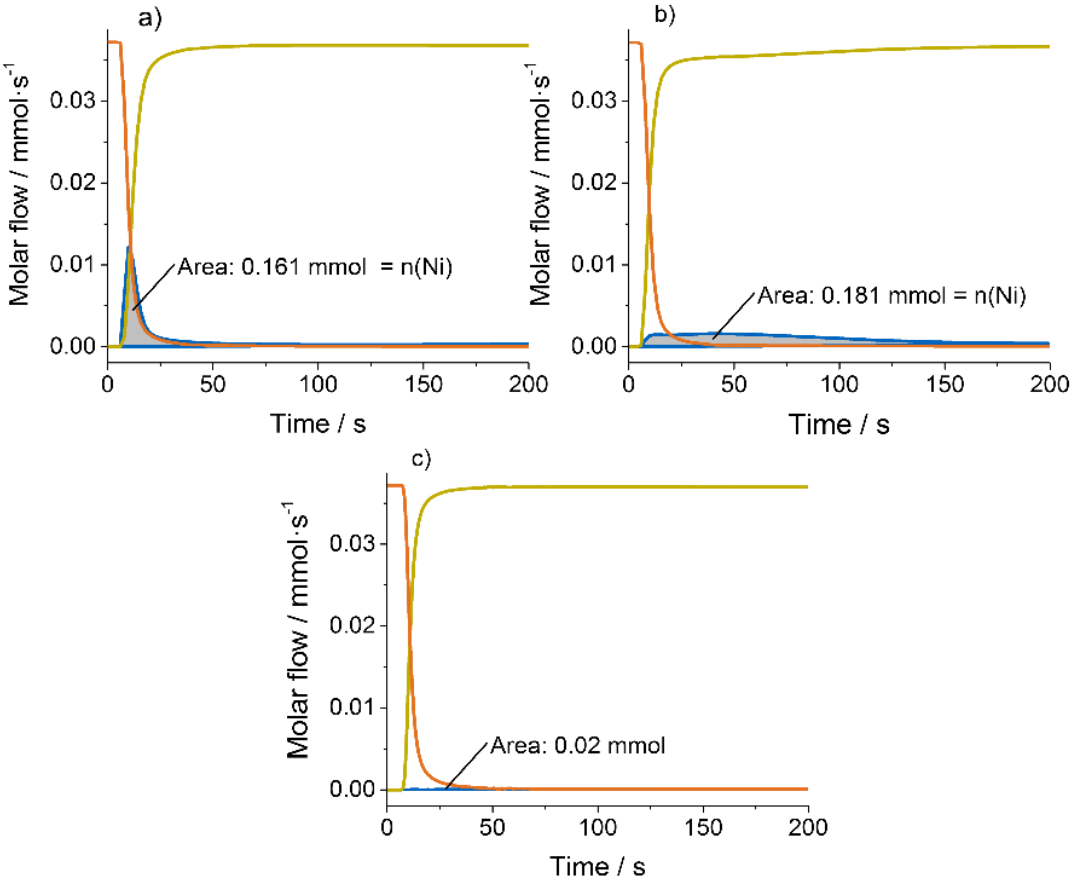

Figure S3.3: CO evolution (blue line) while switching from He (orange line) to CO_2 (green line) at 800°C over Ni/ZrO_2 (a), Ni/SiO_2 (b) and ZrO_2 (c).

3.7 Literature

1. S. Therdthianwong, C. Siangchin and A. Therdthianwong, *Fuel Process. Technol.*, 2008, **89**, 160-168.
2. M. C. J. Bradford and M. A. Vannice, *Catal. Rev.*, 1999, **41**, 1-42.
3. G. S. T. Council, http://www.gasification-syngas.org).
4. M. S. Fan, A. Z. Abdullah and S. Bhatia, *Chemcatchem*, 2009, **1**, 192-208.
5. S. Arora and R. Prasad, *Rsc Adv*, 2016, DOI: 10.1039/C6RA20450C.
6. Z. Y. Liu, D. C. Grinter, P. G. Lustemberg, T. D. Nguyen-Phan, Y. H. Zhou, S. Luo, I. Waluyo, E. J. Crumlin, D. J. Stacchiola, J. Zhou, J. Carrasco, H. F. Busnengo, M. V. Ganduglia-Pirovano, S. D. Senanayake and J. A. Rodriguez, *Angew Chem Int Edit*, 2016, **55**, 7455-7459.
7. T. Odedairo, J. L. Chen and Z. H. Zhu, *Catal Commun*, 2013, **31**, 25-31.
8. A. Peters, F. Nouroozi, D. Richter, M. Lutecki and R. Glaser, *Chemcatchem*, 2011, **3**, 598-606.
9. M. Rezaei, S. M. Alavi, S. Sahebdelfar, P. Bai, X. M. Liu and Z. F. Yan, *Appl Catal B-Environ*, 2008, **77**, 346-354.
10. M. Rezaei, S. M. Alavi, S. Sahebdelfar, X. M. Liu, L. Qian and Z. F. Yan, *Energ Fuel*, 2007, **21**, 581-589.
11. N. Wang, W. Z. Qian, W. Chu and F. Wei, *Catal Sci Technol*, 2016, **6**, 3594-3605.
12. J. A. Montoya, E. Romero-Pascual, C. Gimon, P. Del Angel and A. Monzón, *Catal. Today*, 2000, **63**, 71-85.
13. J. M. Wei and E. Iglesia, *J. Catal.*, 2004, **224**, 370-383.
14. J. H. Bitter, K. Seshan and J. A. Lercher, *J. Catal.*, 1998, **176**, 93-101.
15. J. H. Bitter, K. Seshan and J. A. Lercher, *J. Catal.*, 1999, **183**, 336-343.
16. J. H. Bitter, K. Seshan and J. A. Lercher, *Top Catal*, 2000, **10**, 295-305.
17. J. Lercher, J. Bitter, W. Hally, W. Niessen and K. Seshan, *Studies in Surface Science and Catalysis*, 1996, **101**, 463-472.
18. M. W. Hahn, M. Steib, A. Jentys and J. A. Lercher, *J Mater Chem A*, 2014, **2**, 13624-13634.
19. O. Muller, D. Lutzenkirchen-Hecht and R. Frahm, *Rev Sci Instrum*, 2015, **86**.
20. B. Ravel and M. Newville, *J Synchrotron Radiat*, 2005, **12**, 537-541.
21. J. J. Rehr, J. J. Kas, F. D. Vila, M. P. Prange and K. Jorissen, *Phys. Chem. Chem. Phys.*, 2010, **12**, 5503-5513.
22. S. R. Bare, S. D. Kelly, B. Ravel, N. Greenlay, L. King and G. E. Mickelson, *Phys. Chem. Chem. Phys.*, 2010, **12**, 7702-7711.
23. Y.-g. Chen and J. Ren, *Catal Lett*, 1994, **29**, 39-48.
24. V. M. Gonzalez-Delacruz, R. Pereniguez, F. Temero, J. P. Holgado and A. Caballero, *Acs Catal*, 2011, **1**, 82-88.
25. M. Montes, C. Penneman de Bosscheyde, B. K. Hodnett, F. Delannay, P. Grange and B. Delmon, *Appl Catal*, 1984, **12**, 309-330.
26. C.-j. Liu, J. Ye, J. Jiang and Y. Pan, *Chemcatchem*, 2011, **3**, 529-541.
27. G. Mountjoy, D. M. Pickup, R. Anderson, G. W. Wallidge, M. A. Holland, R. J. Newport and M. E. Smith, *Phys. Chem. Chem. Phys.*, 2000, **2**, 2455-2460.
28. Y. Nagai, T. Yamamoto, T. Tanaka, S. Yoshida, T. Nonaka, T. Okamoto, A. Suda and M. Sugiura, *Catal Today*, 2002, **74**, 225-234.
29. Y. Nagai, T. Yamamoto, T. Tanaka, S. Yoshida, T. Nonaka, T. Okamoto, A. Suda and M. Sugiura, *Top Catal*, 2008, **47**, 137-147.
30. T. Yamamoto, *X-Ray Spectrom*, 2008, **37**, 572-584.
31. M.-C. Silaghi, A. Comas-Vives and C. Copéret, *Acs Catal*, 2016, **6**, 4501-4505.
32. M. M. Makri, M. A. Vasiliades, K. C. Petallidou and A. M. Efstathiou, *Catal. Today*, 2016, **259, Part 1**, 150-164.
33. A. Wolfbeisser, O. Sophiphun, J. Bernardi, J. Wittayakun, K. Föttinger and G. Rupprechter, *Catal. Today*, 2016, **277, Part 2**, 234-245.

34. V. Y. Bychkov, O. V. Krylov and V. N. Korchak, *Kinet. Catal.*, 2002, **43**, 86-94.
35. D. G. Blackmond and E. I. Ko, *J. Catal.*, 1985, **96**, 210-221.
36. J. B. Peri, *J. Catal.*, 1984, **86**, 84-94.
37. K. Coulter, X. P. Xu and D. W. Goodman, *J. Phys. Chem-Us*, 1994, **98**, 1245-1249.

4 Gasification of carbon deposits for dry reforming of methane

The removal of carbon deposits over a Ni/ZrO_2 catalyst after dry reforming of methane at 800°C was studied to reveal the influence of the gasification agent (CO_2, O_2 and N_2O) on the structural properties of the metal particles during catalyst regeneration. Only CO_2 restored the initial activity, while gasification of coke with O_2 and N_2O led to deactivation of the catalyst. EXAFS analysis combined with highly time resolved XANES showed that the deactivation of the catalysts observed after regeneration with O_2 and N_2O can be related to sintering of the metal particles. This increase in particle size is attributed to the high oxidation rate and the related temperature increase of the metal particles under exothermic regeneration conditions with O_2 and N_2O, while the endothermic regeneration with CO_2 is slower and thermally less demanding for the metal particles.

4.1 Introduction

Methane dry reforming, i.e. the reaction of CO_2 with CH_4 to CO and H_2 is an important route to produce syngas with a H_2/CO ratio close to one. Transition metals including Ru, Rh, Pt, Co and Ni are active in methane dry reforming,[1] among them Ni and Co came in the field of interest due to their lower costs compared to noble metal based catalysts. Due to the strong endothermicity of the DRM reaction, high reaction temperatures of 600 – 800°C are required to achieve sufficient conversion levels, which pose several challenges for the design of an active and stable catalyst in methane dry reforming. At high reaction temperatures, metal sintering is a significant issue.[2] There are some approaches to limit metal sintering such as using a support with enhanced metal support interaction e.g., ZrO_2 or CeO_2 [2-5], or coating of the Ni particle itself with a porous layer of metal oxides.[6] As the chemical composition of the feed gas is in a range where the formation of carbonaceous species is thermodynamically feasible, several concepts have been developed to mitigate deactivation from coke deposition. One way is to decrease carbon formation rates via the use of bimetallic catalysts. Kim et al. explored bimetallic NiFe catalysts supported on a $Mg_xAl_yO_z$ matrix, [7] and it has been stated that FeO present in the Ni/Fe alloy particles under reaction conditions participates in a redox mechanism providing labile oxygen to enhance carbon removal. Another way to increase oxygen availability at the catalyst surface is to use mixed oxides like $Ce_{1-x}Zr_xO_2$. Wolfbeisser et al. [5] have shown that the addition of Ce to the ZrO_2 support strongly decreases the carbon formation, as the increased concentration of Ce at the interface of metal and support increases the oxygen density around the Ni particle. We described in chapter 3 that such an effect can also be achieved by exposing a ZrO_2 supported Ni catalyst to pure CO_2, which on the one hand removes the carbon species from the surface, but on the other hand creates labile oxygen species by the decomposition of carbonate intermediates formed on oxygen defect sites on the support. Although these studies have shown that the rate of carbon deposition can be diminished, once deposited, carbon has to be removed periodically by oxidative treatments[8] which pose a challenge in itself, as most of the oxidation reactions are exothermic and the heat generated could lead to metal sintering.

Therefore, the aim of this work was to compare exothermic and endothermic regeneration routes using CO_2, O_2 and N_2O as reactants for gasification of carbon deposits. We will combine highly time resolved X-ray absorption spectroscopy with transient kinetic analysis to show that the oxidation kinetics of a Ni particle itself plays a crucial role in the regeneration of a spent catalyst for methane dry reforming.

4.2 Experimental

4.2.1 Catalyst preparation

The catalyst for this study was prepared according to reference [9] using rccc-5,11,17,23-tetrahydroxy-2,8,14,20-tetra(n-ndecyl)resorc[4]arene (pyrogallol[4]arene, obtained from the group of Prof. Tiefenbacher) to stabilize small metals particles in the arene nano capsules during synthesis. For that purpose, $Ni(NO_3)_2 \cdot 6H_2O$ was added under stirring to a chloroform (Sigma, ≥ 99.9 %) saturated aqueous solution containing the nanocapsules. After stirring for 2 h the desired amount of ZrO_2 (Mel chemicals, XZO1501/03) was added as a support to obtain a catalyst with 12 wt. % Ni loading. The obtained solution was aged for 24 h before removing the solvent by filtration. After impregnation the catalyst was dried at 100°C for 12 h, calcined in air at 500°C for 2 h (flow rate: 100 mL·min^{-1}) and reduced with H_2 at 600°C (heating rate of 0.5 K·min^{-1}) for 2 h (flow rate: 100 mL·min^{-1}).

4.2.2 Activity measurements

The catalyst was placed in a quartz reactor (7 mm diameter) and reduced with 20 vol.% H_2 in N_2 for 1.5 h at 600°C before DRM reaction. The reactant gases consisted of 25 vol.% CH_4 (99.995 vol.%), 25 vol.% CO_2 (99.995 vol.%) and 50 vol.% N_2 (99.999 vol.%) with a total flow of 100 mL·min^{-1}. After 90 minutes of reaction, the product gas was flushed out with N_2, followed by gasification of the deposited carbon in 10 vol.% O_2, CO_2 or N_2O in N_2. The regeneration step was followed by a second reaction cycle. Reaction products were analyzed online by GC and GCMS.

4.2.3 Temperature programmed oxidation

The temperature programmed oxidation of the deposited coke was performed in a Mettler Toledo TGA/DSC balance. The catalyst was heated up to 800°C (5 K·min^{-1}) in a flow of 10 vol.% O_2 (99.995 vol.%) in N_2 with a total flow of 40 mL·min^{-1}. The reaction products were analyzed online by mass spectrometry using a Pfeiffer Omnistar GSD 320.

4.2.4 X-ray absorption spectroscopy

Time resolved X-ray absorption spectra were measured at the SuperXAS beamline at the SLS in Villigen. All data were recorded in transmission mode at the Ni K-edge at 8333 eV with a channel-cut Si(111) monochromator operated at an oscillation frequency of 30 Hz. Analysis of the QEXAFS data was carried out with the JAQ software.[10] All other XAS experiments were carried out at the beamline P65 at DESY, Hamburg.

The in situ experiments were conducted in a quartz glass capillary (WJM Glas, 1 mm diameter, 20 µm wall thickness). The pressed catalysts (80 – 120 µm) were diluted with BN

and the catalyst bed (4 mm length) was fixed in the capillary with two plugs made of quartz wool. The capillary was placed in the sample holder as described above. The flow of the reactant gasses during the experiment was kept constant at 20 mL·min^{-1}. After flushing the catalysts with He at room temperature, the catalysts were heated up to 600°C (10 K·min^{-1}) in He and the reduction was performed in a mixture of 10 vol. % H_2 in He for 1.5 h. The catalysts were heated to 800°C in He and the reaction was carried out using 25 vol.% CH_4 and 25 vol.% CO_2 in He. The regeneration was carried out in 10 vol.% of O_2, CO_2 or N_2O in He after flushing the capillaries with He. After regeneration, a second reaction cycle was performed.

Analysis of the EXAFS data was carried out with Athena and Artemis software from the IFEFFIT [11] package using FEFF6 to calculate the phase shift and amplitude functions for the single and multiple scattering contributions.[12] The XAS spectra were calibrated to 8333 eV using a Ni foil as reference and the edge step was normalized to one. XANES were fitted by linear combination analysis using NiO and reduced Ni as references. After background removal the oscillations were weighted with k^3 and Fourier transformed within the limit of k = 2.5-12.0 Å^{-1}. The local environment of the Ni atoms was determined by fitting the oscillations in k-space including single and multiple scattering paths calculated using FEFF.[13]

4.3 Results and discussion

4.3.1 Characterization

The coordination number and the corresponding dispersion was calculated from EXAFS after in situ reduction and cooling to 30°C (Figure 4.1 A). The absence of Ni-O contributions confirms that the catalyst was fully reduced. Fitting of the EXAFS results a Ni-Ni coordination number of 9.6, which corresponds to an octahedral shaped particle with five shells having a diameter of 1.9 nm and a dispersion of 52%.

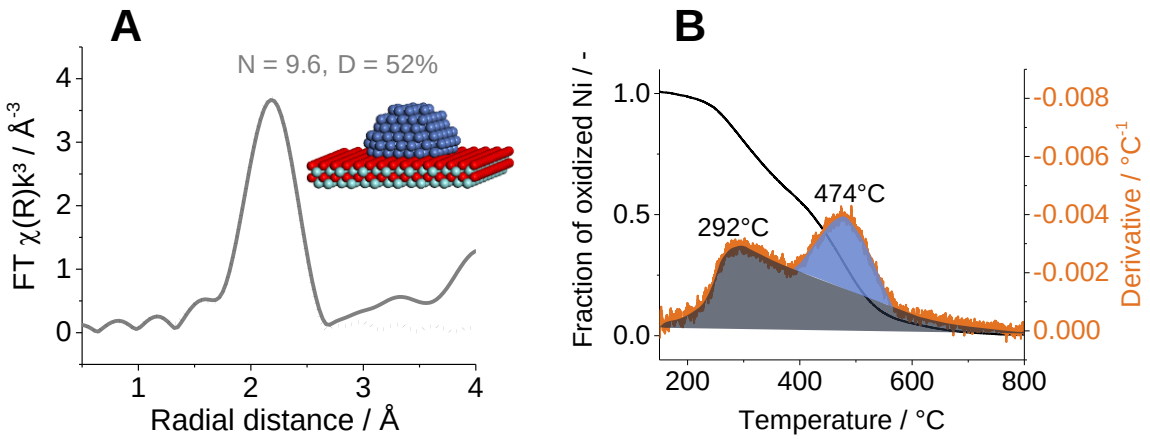

Figure 4.1: Fourier transformed EXAFS (A) at the Ni K-edge recorded at 30°C (grey line), first shell fit of the EXAFS (dotted black line) and (B) Linear combination analysis (black line) and corresponding derivative during temperature programmed reduction of a calcined sample followed by QXANES.

To further explore the reduction properties of the catalyst, temperature programmed reduction (5 K·min^{-1}) of the calcined sample was followed by quick-XANES and the changes in the oxidation state as a function of temperature were obtained by linear combination analysis using bulk NiO and Ni foil as references (black line in Figure 4.1 B). After calcination at 500°C the catalyst was fully oxidized, while treatment in 10% H_2 in He resulted in a reduction of the catalyst to metallic Ni. The rate of reduction was obtained by deriving the fraction of reduced species over the time. The TPR profile obtained reveals two maxima indicating the presence of two Ni species with different interaction to the support. To quantify the amount of each species, the peaks were fitted as visualized in Figure 4.1 B. The TPR indicates that 70% of the Ni species were reduced at low temperatures around 292°C (dark blue part), while the remaining fraction could only be reduced at higher temperatures (above 400°C, light blue part). The latter value fits well to the number of Ni atoms, which are in direct contact to the support (30% of the Ni atoms in light blue Figure 4.1 B) assuming a dispersion of 52% and an octahedral particle shape. Therefore, the second maximum at 474°C can be attributed to Ni atoms in the vicinity of metal and support (light blue in Figure 4.1 B). These results are in agreement with Li et al. [14] who observed similar reduction temperatures for nano-sized Ni particles supported on ZrO_2. Furthermore the formation of strong chemical

bonds between metal and support and the according reduction properties have been confirmed by DFT calculation.[15]

4.3.2 Catalytic activity and gasification of carbon deposits

The turnover rates for CH_4 conversion at 800°C as a function of time on stream are shown in Figure 4.2. In all three experiments, the amount of catalyst in the reactor was the same. After 90 minutes of dry reforming a deactivation to about 50% of the initial activity was overserved, which required a regeneration under oxidative conditions for 90 minutes in 10% O_2 in N_2, 10% CO_2 in N_2 or 10% N_2O in N_2 at 800°C.

After the oxidative treatment only regeneration in CO_2 restored the initial activity, while catalyst regenerated in N_2O reached 80% and in O_2 only 60% of the initial activity.

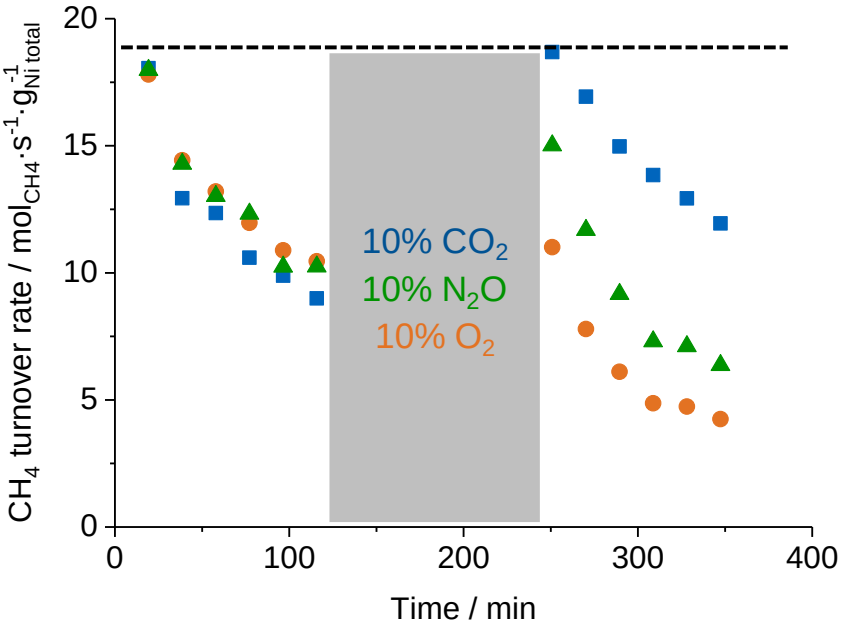

Figure 4.2: CH_4 turnover rates of a 12% Ni/ZrO_2 catalyst with intermitted regeneration in 10% CO_2 (blue squares), 10% N_2O (green triangles) and 10% O_2 (orange circles).

To further explore the deactivation observed in the first reaction cycle, temperature programmed oxidation of the spent catalyst after the first reaction cycle was performed (Figure 4.3 A and 4.3 B). To differentiate between the weight loss due to carbon removal and increase in weight caused by oxidation of the Ni particles, the TPO profiles in Figure 4.3 A and B were corrected using a blank experiment where only the fresh pre-reduced catalyst was used (Figure 4.3 C). Please note that the reduced Ni particles were already oxidized at 285°C, whereas carbon deposits were oxidized at higher temperatures

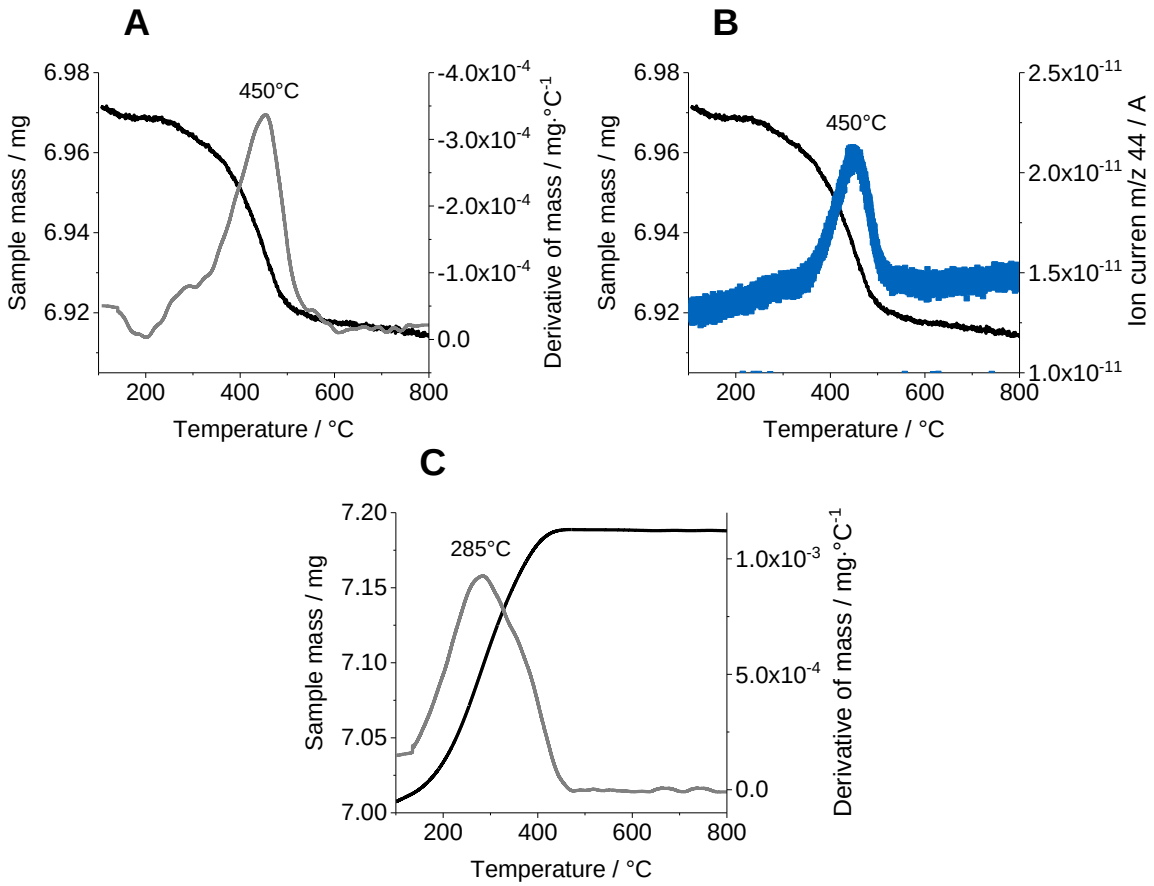

Figure 4.3: Temperature programmed oxidation of the spent catalyst after the first reaction cycle (A, black curve), corresponding derivative (A, grey curve), intensity of MS signal m/z 44 (B, blue curve), temperature programmed oxidation of the reduced catalyst (C, black curve) and corresponding derivative (C, grey curve).

The rate of oxidation, calculated from the derivative of the weight loss as function of time, reflects the nature of the carbon deposits. Zhang et al. [16] have shown, that carbon which is oxidized between 400 and 500°C is encapsulating carbon, while a oxidation temperature higher than 600°C can be related to carbon whiskers. As the maximum of oxidation rate over the sample studied was at 450°C, we attribute the weight loss to the removal of encapsulating carbon. Using the dispersion of 52% (obtained by EXAFS analysis) to determine the number of Ni surface sites and the amount of carbon formed, the number of sites, previously covered by encapsulating carbon can be calculated by:

$$\frac{n(sites\ covered\ by\ carbon)}{n(sites\ at\ the\ surface)} = \frac{n(C)}{n(Ni_{surface})} = \frac{\frac{\Delta m(TGA)}{M(C)}}{n(Ni_{total}) \cdot D} = \frac{3.3\ \mu mol}{6.2\ \mu mol} = 0.53$$

With M(C) molar mass of carbon, D metal dispersion and $\Delta m(TGA)$ mass loss during TPO

This calculation reveals that 53% of the exposed Ni surface atoms were covered with carbon before regeneration and were thus inaccessible for CH_4, which perfectly agrees with the decrease in CH_4 turnover rate from 18 to 10 $mol \cdot s^{-1} \cdot g_{Ni}^{-1}$ after 90 min of DRM. Therefore, we attribute the deactivation observed during dry reforming to the blocking of active Ni sites due to the formation of encapsulating carbon.

To further explore structural changes of the Ni particles during the oxidative treatment, we conducted in situ X-ray absorption spectroscopy at the Ni K-edge in transmission mode. To ensure equal conditions for every sample, the novel fivefold capillary cell was used for these measurements. The XANES during the first reaction cycle, the subsequent oxidation and the second reaction cycle are compared in Figure 4.4. As concluded from the position of the absorption edge and the height of the white line, Ni is fully reduced under DRM conditions.

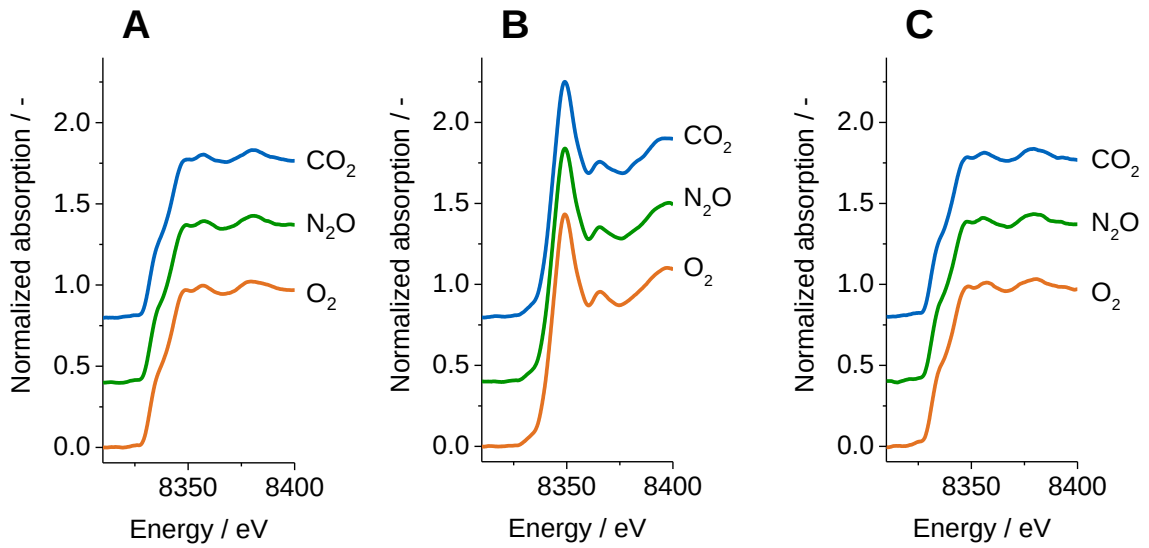

Figure 4.4: XANES of a Ni/ZrO_2 catalyst recorded at 800°C during switching from reaction atmosphere (A) to the oxidizing agent (B) and reaction atmosphere again (C).

Switching to regeneration conditions in oxidative atmosphere the increase in the white line intensity and a shift of the absorption edge indicates formation of NiO. Comparing the height and shape of the white line with (bulk) NiO we conclude, that all three oxidants were able to fully oxidize Ni^0 to Ni^{2+} at the reaction conditions chosen for this study. Switching back to DRM reaction conditions (reducing atmosphere) results in a decrease in white line attributed to a reduction of the Ni particles from Ni^{2+} to Ni^0. To deeper analyze structural changes of the Ni particles, EXAFS were taken before reaction (Figure 4.1 B), after the first DRM cycle (Figure S4.2), after the oxidative treatment and after 1 min of DRM in the second cycle to reduce the previously oxidized catalyst again. While capillaries 1 - 3 were used to study the

influence of the oxidizing agent (CO_2, O_2 and N_2O) on the structure of the Ni particles, capillary 4 was only flushed with Helium (after the initial reduction) to exclude thermal effects on the size of the Ni particles. In order to exclude changes in particle size caused by the dry reforming reaction itself, the catalyst in capillary 5 was not regenerated during the cycles and therefore, the DRM reaction was continued (Figure S4.1).

Table 4.1: Coordination numbers obtained by EXAFS analysis, corresponding dispersions and normalized CH_4 rates.

	N -	**D** %	**Normalized CH_4 rate** $mol_{CH4} \cdot s^{-1} \cdot g_{Ni,surface}^{-1}$
fresh	9.6	52	36
CO_2	9.6	53	35
N_2O	10.2	43	35
O_2	10.7	32	35

The resulting fits of the EXAFS including all fitting parameters can be found in the supporting information. The dispersion of the Ni particles did not change during the removal of carbon deposits in CO_2 (shown in Table 4.1), while after regeneration with N_2O and with O_2 the dispersion strongly decreased. Please note that the dispersion of the catalyst exposed to He and the one exposed to dry reforming atmosphere did not change. To confirm that the deactivation caused by the oxidative treatment results from sintering of the Ni particles, the turnover rates after the oxidation cycle were normalized to the number of accessible sites (Table 4.1). This calculation had to be carried out using the activity just after switching to DRM reaction conditions, as the amount of carbon blocking the active sites is supposed to be negligible at this time. As all TOF were equal (within limits of accuracy) we attribute the differences in activity after the oxidative treatment to the decreased number of active surface sites available for CH_4 conversion resulting from sintering of the metal particles. In order to differentiate the oxidation of the particle and the oxidation of carbon deposits, which occur in parallel during the regeneration cycle, we exposed the catalyst to reducing atmosphere followed by an oxidation in O_2 (Figure 4.5 A). Under these conditions only the Ni particles were oxidized during the exposure to O_2 as no carbon has been deposited before.

Figure 4.5 B compares the results of this experiment with the results of the experiment displayed in Figure 4.2.

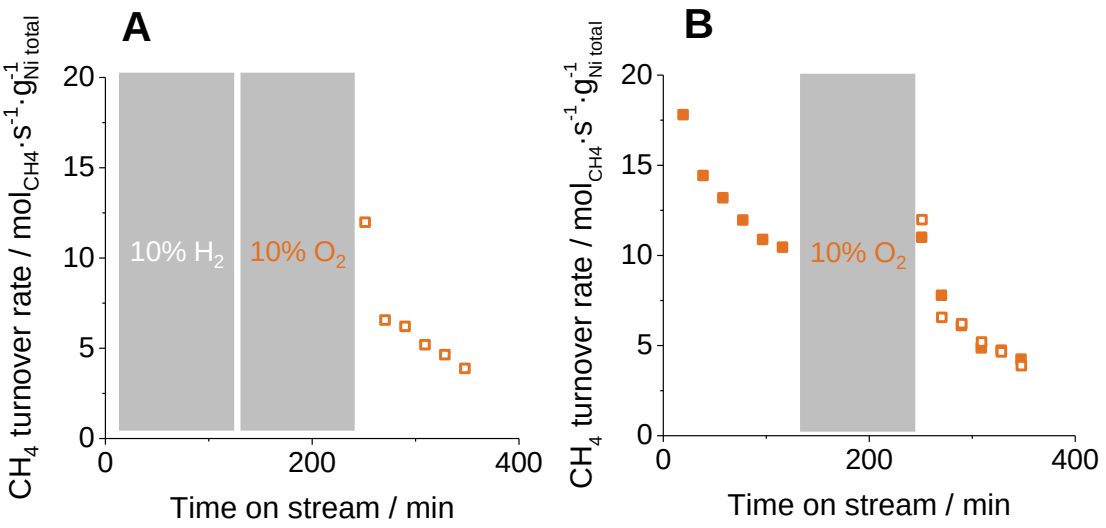

Figure 4.5: CH_4 turnover rates without DRM in a first cycle (A, empty squares) and comparison of this data to the data with DRM in the first cycle (B, filled squares).

As the CH_4 turnover rates after the oxidative treatment were equal for both cases, we conclude that the oxidation of the particle was responsible for the sintering of the particles, while the combustion of coke does not affect the particle agglomeration. The difference in the reaction enthalpies for the oxidation of Ni are compiled in Table 4.2. It should be noted that the reaction with CO_2 is slightly endothermic, while the reaction with the other two oxidation agents are highly exothermic.

Table 4.2: Reaction equations and corresponding reaction enthalpies for the oxidation of Ni with O_2, CO_2 and N_2O (calculations done with HSC 6.0).

	Reaction equation	Reaction enthalpy
CO_2	$Ni + CO_2 \rightleftharpoons NiO + CO$	$\Delta H^0 = +47\ kJ \cdot mol^{-1}$
O_2	$Ni + 0.5\ O_2 \rightleftharpoons NiO$	$\Delta H^0 = -235\ kJ \cdot mol^{-1}$
N_2O	$Ni + N_2O \rightleftharpoons NiO + N_2$	$\Delta H^0 = -319\ kJ \cdot mol^{-1}$

Heat evolution during the reaction can be estimated by a simplified heat balance:

$$\dot{Q}_{accumulation} = r_{oxidation} \cdot \Delta H = -\frac{dc_{NiO}}{dt} \cdot \Delta H$$

The reaction conditions of 800°C, as well as the heat transport to the environment of the Ni particles (ZrO_2 support, SiC dilution) make a detailed calculation of the particle temperature complicated, nevertheless, we assume in first instance that the particle temperature will be proportional to the accumulated heat flux.

To determine the rate of oxidation, QEXAFS at the Ni K-edge were collected with a time resolution of 30 Hz (Figure 4.6). After in situ reduction in 10% H_2 in He for 90 minutes at 600°C, the fully reduced catalyst was flushed with He followed by the exposure to the different oxidizing agents.

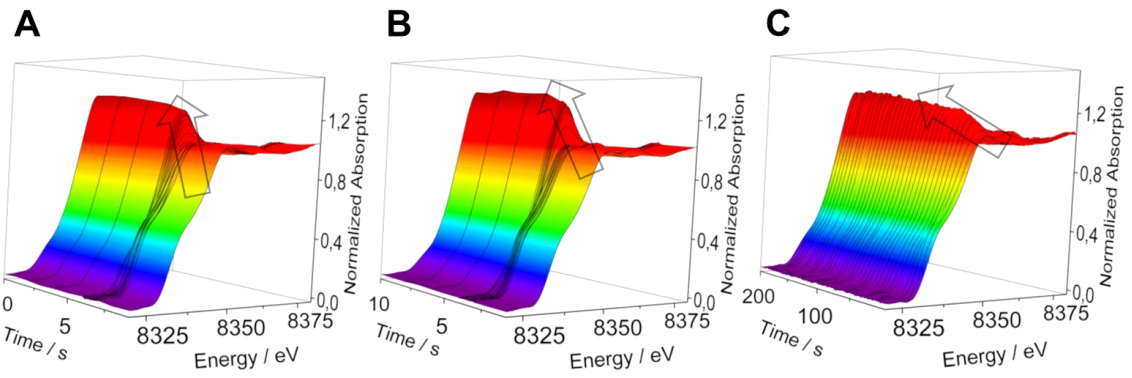

Figure 4.6: QEXAFS during switching from He to 10% O_2 (A), 10% N_2O (B) and 10% CO_2 (C) at 800°C.

After the initial reduction, the catalyst was fully reduced as concluded from the position of the edge at 8333 eV and from the shape of the XANES at the Ni K-edge. Exposing the catalysts to an oxidizing agent resulted in an increase of the white line intensity (marked by an arrow in Figure 4.6) and a shift of the absorption edge. Please note the different time scale used in Figure 4.6 C for the significantly slower oxidation process with CO_2. The oxidation state of Ni was determined by linear combination analysis using Ni foil and bulk NiO as references. The changes in the oxidation state as function of time are compared in Figure 4.7 A.

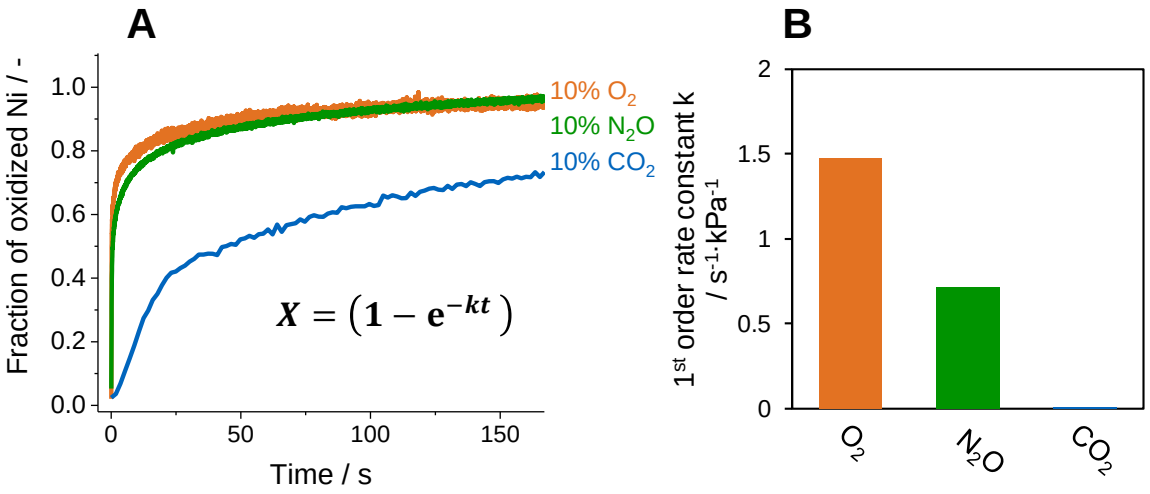

Figure 4.7: (A) Variation of Ni^{2+} concentration deduced by linear combination fitting of QEXAFS data while switching from He to 10% CO_2 (blue line) in He, 10% N_2O in He (green line) and 10% O_2 in He (orange line) and (B) analysis of the 1st order rate constants.

The rates of the oxidation reaction were fitted with a 1st order rate approach [17] and the resulting first order rate constants normalized to the partial pressure of the corresponding gas are displayed in Figure 4.7 B. The oxidation of the particle in O_2 (k_{O2} = 1.47 s^{-1}·kPa^{-1}) was the fastest among the three oxidation reactions, whereas the oxidation with N_2O (k_{N2O} = 0.72 s^{-1}·kPa^{-1}) was slightly slower and with CO_2 significantly slower (k_{CO2} = 0.004 s^{-1}·kPa^{-1}). This slower processes result from the slower decomposition of the molecules on the metal surface or at the metal support interface. In case of CO_2 the dissociation at the metal support interface enables the release of oxygen species via the reaction $CO_2 \rightleftharpoons CO^* + O^*$, which is faster than the reaction on the metallic Ni particles as observed by Steib et al. (see chapter 3). These results show that the dissociation of O_2 and N_2O on the Ni surface are faster compared to the dissociation of CO_2. Using the rate constants of oxidation, the heat evolution in the reactor as a function of time can be calculated, which should correspond to the maximum temperature reached in the catalyst bed during the oxidation of the Ni particles (Figure 4.8 A). The heat evolution for the reaction in O_2 at the beginning is the highest, although the reaction enthalpy of this reaction is lower compared to the reaction with N_2O (see Table 4.2). A direct correlation between the changes in metal dispersion and the heat evolution was observed (see Figure 4.8 B), which indicates that the increase in particle size can be attributed to the heat evolution during the oxidation of the Ni particles, while the oxidation of carbon deposits did not affect the particle agglomeration.

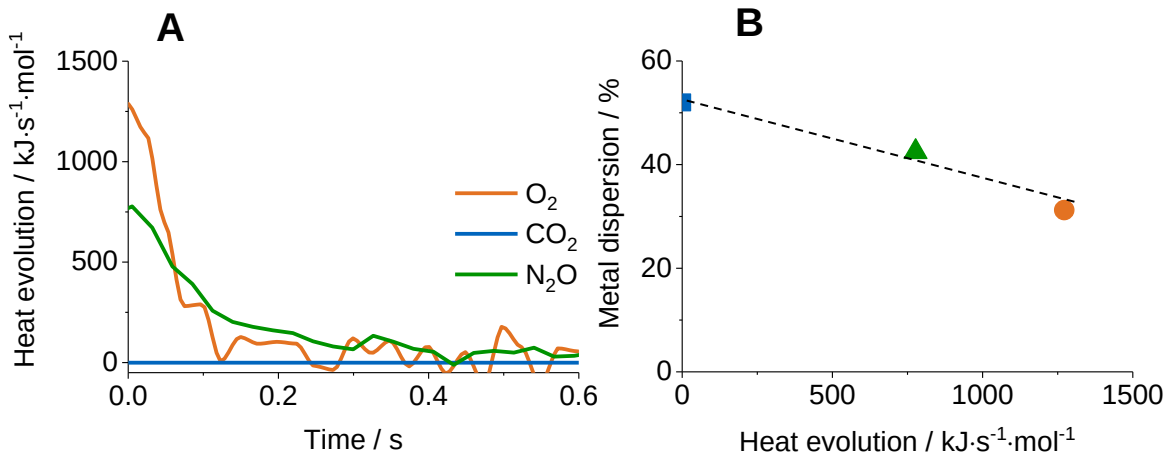

Figure 4.8: Heat evolution over time (A) and correlation of the metal dispersion and the maximum heat evolution (B).

Thus we further conclude that the oxidation of the Ni particle occurs at a faster rate than the oxidation of the carbon deposits, which is supported by the fact that Ni is oxidized at lower temperatures in the temperature programmed oxidation (Figure 4.3) compared to the oxidation of carbon. This observation is consistent with literature, as Trimm et al. observed that the rate of carbon removal from fully encapsulated Ni particles was enhanced as soon as metal was accessible to dissociate O_2.[18] The higher rate of oxidation of Ni compared to carbon deposits in case of O_2 is caused by a higher barrier for the dissociation of molecular O_2 on carbon than on Ni, as shown by Wang et al. using DFT calculations.[19] Therefore, we propose a mechanism of kinetically controlled coke removal and oxidation of carbon deposits with N_2O and O_2 as depicted in Figure 4.9. The dissociation occurs at a higher rate on the Ni surface than on carbon, leading to a higher concentration of oxygen atoms on Ni. After the formation of a NiO shell, the metal core of the particle is continuously oxidized according to the Carbera-Mott model.[20, 21] After this process, the dissociation occurs on the NiO surface and atomic oxygen can migrate to the carbon deposits leading to the formation of CO_2 which in turn desorbs. From the current results we can only speculate that N_2O follows the same mechanism as O_2. The oxidation mechanism of CO_2 is slightly different compared to N_2O and O_2, as CO_2 is mainly activated at the metal at the metal support interface. The transiently formed carbonates decompose to CO and a labile oxygen species which in turn oxidize carbon and the Ni particle. As the oxidation occurs at a much slower rate, we propose that the rate determining step is the dissociation of CO_2 at the metal support interface.

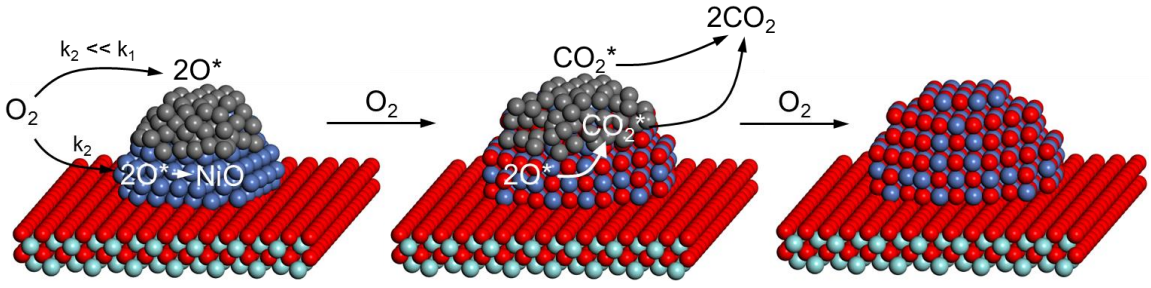

Figure 4.9: Schematic representation of the oxidation mechanism of a coked Ni/ZrO_2 catalyst.

4.4 Conclusions

In the present study, we compare three oxidation agents to remove carbon deposits for dry reforming of methane. We have shown that on Ni/ZrO_2 the formation of encapsulating carbon is the main reason for catalyst deactivation during methane dry reforming, whereas sintering of the metal particles at elevated temperature of the dry reforming reaction did not occur. Three oxidation agents, O_2, CO_2 and N_2O, were used for coke removal and the changes in the particle size after regeneration clearly revealed that CO_2 can be applied for catalyst regeneration without inducing sintering of the metal particles. As this reaction is endothermic, excessive agglomeration of the particles can be avoided, while the exothermic oxidation reactions with O_2 and N_2O led to a strong deactivation of the catalysts directly related to the loss of surface atoms. The direct correlation of the dispersion after regeneration and the heat evolution caused exclusively by the oxidation of the Ni particles allowed to conclude, that the oxidation of the particle itself occurred faster than the oxidation of carbon deposits and is therefore responsible for the heat induced sintering.

4.5 Associated content

Publication

This chapter is based on an article planned for submission (Matthias Steib, Andreas Jentys and Johannes A. Lercher)

Contributions

Matthias Steib did main contributions in kinetic experiments, EXAFS measurements, data analysis and manuscript preparation. Andreas Jentys was the co-advisor and Johannes A. Lercher the principal investigator.

Acknowledgements

This work was financially supported by the BMBF under the project ZeitKatMat. The X-Ray absorption experiments were performed on the SuperXAS beamline at the Swiss Light Source, Paul Scherrer Institut, Villigen, Switzerland. The authors gratefully acknowledge the beamline scientist Maarten Nachtegaal for his help during the beamtime. Parts of this research were carried out at the light source PETRA III at DESY, a member of the Helmholtz Association (HGF). We would like to thank Edmund Welter for assistance in using beamline P65.

4.6 Appendix

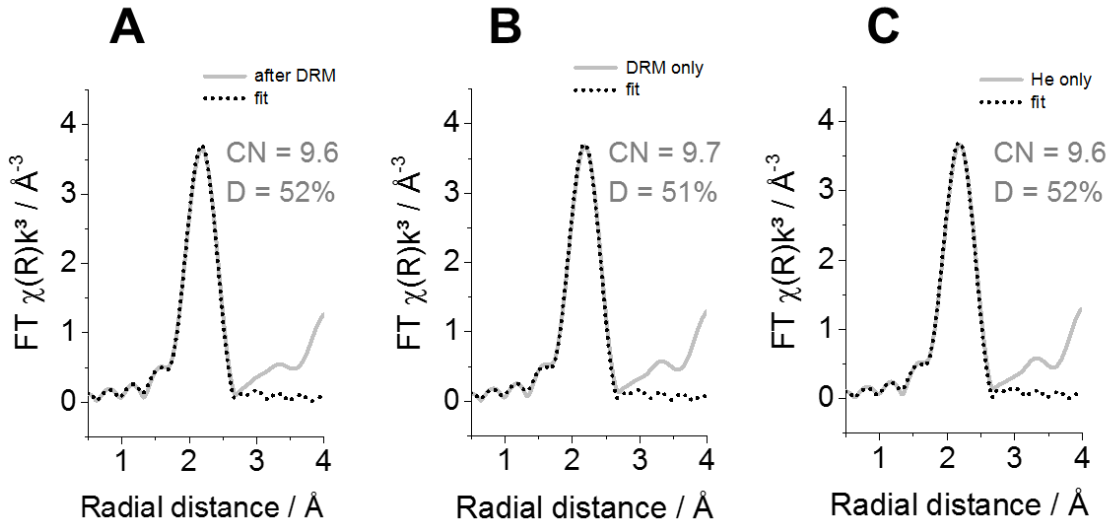

Figure S4.1: Fourier transformed EXAFS and corresponding fits (dotted lines) recorded at 30°C after the first DRM cycle (A) after 360 minutes DRM (B) and after 360 minutes in He at 800°C (C).

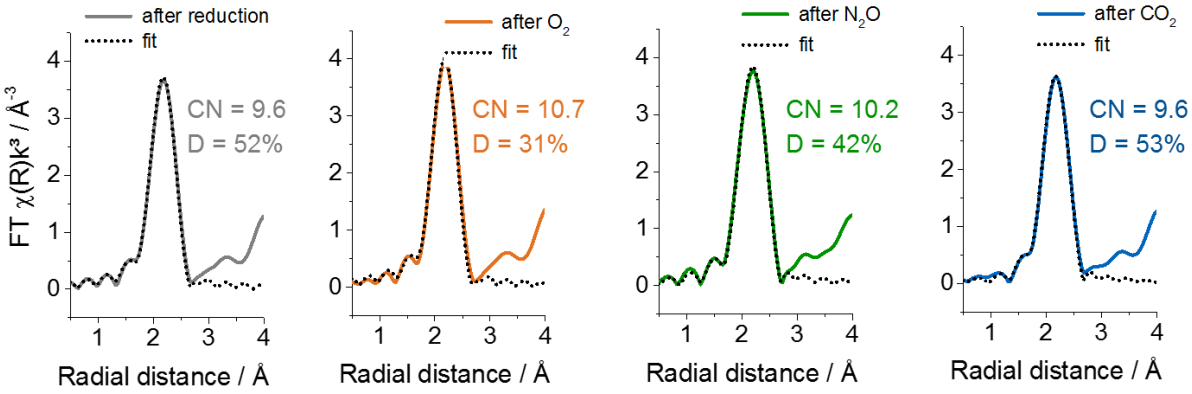

Figure S4.2: Fourier transformed EXAFS and corresponding fits (dotted lines) recorded at 30°C.

Table S4.1: Fit results of a Ni/ZrO_2 catalyst during cycle experiments and reference materials.

	Ni-Ni				
	N	ΔE_0 [eV]	r [Å]	σ^2 [Å²]	d [nm]
Ni foil	12.0	7.73	2.489	0.0065	
fresh	9.6	5.89	2.486	0.0059	1.9
After O_2	10.7	5.79	2.485	0.0062	3.2
After CO_2	9.6	5.94	2.487	0.0059	1.9
After N_2O	10.2	8.89	2.491	0.0057	2.2-2.5
After He	9.6	5.90	2.489	0.0059	1.9
After DRM	9.6	5.89	2.490	0.0058	1.9
After 100 min DRM	9.6	5.88	2.489	0.0062	1.9

4.7 Literature

1. R. K. Singha, A. Yadav, A. Agrawal, A. Shukla, S. Adak, T. Sasaki and R. Bal, *Applied Catalysis B: Environmental*, 2016, **191**, 165-178.
2. Z. Y. Liu, D. C. Grinter, P. G. Lustemberg, T. D. Nguyen-Phan, Y. H. Zhou, S. Luo, I. Waluyo, E. J. Crumlin, D. J. Stacchiola, J. Zhou, J. Carrasco, H. F. Busnengo, M. V. Ganduglia-Pirovano, S. D. Senanayake and J. A. Rodriguez, *Angew. Chem. Int. Edit.*, 2016, **55**, 7455-7459.
3. H. Ay and D. Üner, *Applied Catalysis B: Environmental*, 2015, **179**, 128-138.
4. J. A. Montoya, E. Romero-Pascual, C. Gimon, P. Del Angel and A. Monzón, *Catal. Today*, 2000, **63**, 71-85.
5. A. Wolfbeisser, O. Sophiphun, J. Bernardi, J. Wittayakun, K. Föttinger and G. Rupprechter, *Catal. Today*, 2016, **277, Part 2**, 234-245.
6. J. W. Han, C. Kim, J. S. Park and H. Lee, *Chemsuschem*, 2014, **7**, 451-456.
7. S. M. Kim, P. M. Abdala, T. Margossian, D. Hosseini, L. Foppa, A. Armutlulu, W. van Beek, A. Comas-Vives, C. Copéret and C. Mueller, *J Am Chem Soc*, 2017.
8. L. S. Lobo, *Catalysis Reviews*, 2013, **55**, 210-254.
9. Y. Lou, M. Steib, A. Jentys and J. A. Lercher, *J Am Chem Soc*, 2017, **to be submitted**.
10. O. Muller, D. Lutzenkirchen-Hecht and R. Frahm, *Rev Sci Instrum*, 2015, **86**.
11. B. Ravel and M. Newville, *J Synchrotron Radiat*, 2005, **12**, 537-541.
12. J. J. Rehr, J. J. Kas, F. D. Vila, M. P. Prange and K. Jorissen, *Phys. Chem. Chem. Phys.*, 2010, **12**, 5503-5513.
13. A. Belsky, M. Hellenbrandt, V. L. Karen and P. Luksch, *Acta Crystallogr B*, 2002, **58**, 364-369.
14. S. Li, C. Zhang, Z. Huang, G. Wu and J. Gong, *Chem Commun*, 2013, **49**, 4226-4228.
15. J. Beltrán, S. Gallego, J. Cerdá, J. Moya and M. Munoz, *Phys Rev B*, 2003, **68**, 075401.
16. Z. L. Zhang and X. E. Verykios, *Catal Today*, 1994, **21**, 589-595.
17. J. T. Richardson, R. Scates and M. V. Twigg, *Appl Catal a-Gen*, 2003, **246**, 137-150.
18. D. L. Trimm, *Catal Rev*, 1977, **16**, 155-189.
19. Z. Y. Wang, X. M. Cao, J. H. Zhu and P. Hu, *J. Catal.*, 2014, **311**, 469-480.
20. R. Karmhag, G. A. Niklasson and M. Nygren, *J Appl Phys*, 2001, **89**, 3012-3017.
21. V. P. Zhdanov and B. Kasemo, *Chem Phys Lett*, 2008, **452**, 285-288.

5 Summary

The scope of this thesis was the development of a general approach for stable operation of Ni based catalysts for methane dry reforming. The first chapter describes thermodynamic parameters for dry reforming of methane. It has been shown that the chemical composition of the feed gas (CO_2/CH_4 = 1) favors carbon formation thermodynamically. At atmospheric pressure, slightly increasing the CO_2 partial pressure would diminish carbon formation. Nevertheless, at elevated pressure (30 bar) carbon formation is a more demanding issue, as only the addition of high amounts of water would lead to carbon free operation. Therefore, carbon formation should be reduced with efficient catalyst design. However, once deposited, carbon has to be removed periodically to ensure high reaction rates without deteriorating its activity.

The key for developing this concept is a fundamental understanding of metal support interactions as well as their influence on the activity and stability of the catalyst. The second chapter of this thesis describes the design of a novel fivefold capillary cell for in situ X-ray absorption spectroscopy. Analysis of possible materials (e.g. ceramics, polymers…) has shown that quartz glass capillaries with an outer diameter of 1 mm and a wall thickness from 10 – 30 µm give the highest flexibility with respect to temperature, pressure and edge energy (depending on the active metal of the catalyst). This cell allows the treatment of up to five samples in parallel and enables an efficient usage of highly time-limited synchrotron radiation.

In the third chapter gives insight into the metal support interactions in methane dry reforming. Three different catalysts, Ni/SiO_2, Ni/Al_2O_3 and Ni/ZrO_2 have been prepared and tested for the DRM reaction. After 90 minutes of time on stream, the catalysts were exposed to a stream of 100% CO_2 to remove carbon deposits via the thermally less taxing reverse Boudouard reaction. In the subsequent dry reforming cycle, Ni/ZrO_2 showed a threefold increase in reaction rate whereas the activity of Ni/Al_2O_3 and Ni/SiO_2 further decreased. It has been shown that only ZrO_2 was able to sufficiently stabilize Ni particles during catalysis and regeneration. The increase in rate was caused by the higher concentration of accessible Ni metal sites after exposure to CO_2, while the stability was enhanced by the presence of labile atomic oxygen, which readily oxidizes surface carbon formed during the dissociation of methane.

The fourth chapter focuses on the development of regeneration protocols for spent catalysts in methane dry reforming. Time resolved X-ray absorption spectroscopy has been used to determine oxidation kinetics of nano-sized Ni particles with three different oxidants (CO_2, O_2 and N_2O). The linear correlation of the dispersion after regeneration and the heat flux caused by the oxidation of the Ni particles allowed to conclude, that the oxidation of the particle itself occurred faster than the oxidation of carbon deposits and is therefore responsible for the heat induced sintering of the Ni particles treated with O_2 and N_2O.

In summary, applying these concepts enables in combination with the reducible ZrO_2 support, stable operation of inexpensive Ni catalysts for methane dry reforming.

6 Zusammenfassung

Trockenes Reformieren von Methan liefert Synthesegas mit einem theoretischen H_2/CO Verhältnis von 1, welches beispielsweise als Edukt für den Fischer Tropsch Prozess oder zur Methanol Synthese eingesetzt werden kann. Aufgrund der hohen Gasvolumina, die bei der Synthesegasherstellung umgesetzt werden, ist der Einsatz eines teuren Katalysators auf Edelmetallbasis nahezu nicht rentabel, weshalb Katalysatoren auf Ni Basis in den Vordergrund der Forschung rückten.

Das erste Kapitel dieser Thesis beschreibt thermodynamische Berechnungen auf Grundlage der Minimierung der Freien Gibbs'schen Energie. Es wird gezeigt, dass die chemische Zusammensetzung des Eduktgases entscheidend für die Stabilität von Kohlenstoffablagerungen ist. Bei einem Systemdruck von 1 bar und einer Temperatur von 800°C reicht schon eine geringfügige Erhöhung des CO_2 Partialdrucks aus um die Kohlenstoffablagerung aus thermodynamischer Sicht zu verringern. Industriell werden Methanreformer allerdings bei höheren Drücken betrieben, da diese für die weitere Verarbeitung des Synthesegases benötigt wird. Bei einem Gesamtdruck von 30 bar lassen sich Kohlenstoffablagerungen nicht mehr durch Erhöhung des CO_2 Partialdrucks verhindern. Lediglich die Zufuhr von großen Mengen Wasserdampf verringert die Kohlenstoffablagerung. Sobald sich Kohlenstoff abgelagert hat, muss dieser oxidativ von der Katalysatoroberfläche entfernt werden, was aufgrund der hohen Exothermie vieler Oxidationsreaktionen zusätzlichen Wärmeeintrag und somit Deaktivierung durch Sintern hervorrufen kann. Daher soll in dieser Arbeit ein generelles Konzept entwickelt werden, welches die Regenerierung eines deaktivierten Katalysators ermöglicht, ohne dessen Aktivität (z.B. durch Sintern) zu verringern. Dabei besteht der erste Schritt darin, den Katalysator unter Reaktionsbedingungen (in situ / in operando) zu charakterisieren. Hierfür bietet sich für geträgerte Metallkatalysatoren die Röntgenabsorptionsspektroskopie an.

Das zweite Kapitel dieser Arbeit beschreibt die Auslegung einer neuartigen Kapillarzelle, die es ermöglicht, bis zu fünf Proben gleichzeitig vorzubehandeln und somit den zeitlich sehr beschränkten Zugang zu Synchrotronstrahlung effizient zu nutzen. Die Analyse verschiedener Materialien (z.B. Keramik, Polymere) für die Konstruktion dieser Zelle hat gezeigt, dass Kapillaren aus Quarzglas mit einem Außendurchmesser von 1 mm und einer Wandstärke von 10 – 30 µm am besten geeignet sind, da diese eine hohe Flexibilität in Temperatur, Druck und Kantenenergie erlauben.

Das dritte Kapitel erläutert die Rolle der Metall – Träger Wechselwirkungen für die Aktivität und Stabilität eines Katalysators im Trockenen Reformieren von Methan. Es wurden drei unterschiedliche Katalysatoren, Ni/SiO_2, Ni/Al_2O_3 und Ni/ZrO_2 präpariert und in der DRM Reaktion getestet. Nach 90 minütiger Reaktionszeit wurden alle drei Katalysatoren einem Strom von reinem CO_2 ausgesetzt um die Kohlenstoffablagerungen über die umgekehrte Boudouard Reaktion abzubrennen. Im nachfolgenden Trockenreformierschritt zeigte nur Ni/ZrO_2 eine um einen Faktor 3 höhere Rate als zuvor, die anderen beiden Katalysatoren hingegen deaktivierten weiter. Es wurde gezeigt, dass sich unter CO_2 Atmosphäre an der Grenzfläche zwischen Ni und ZrO_2 Zirkoncarbonate ausbilden, die wiederum eine Restrukturierung der Katalysatoroberfläche ermöglichen. Das Resultat ist ein Katalysator mit dreifach höherer Ni Zentren Zahl, die eine höhere Aktivität bewirken sowie einer um den

Faktor drei angestiegenen Zahl der Zentren an der Grenzfläche zwischen Metall und Träger, die wiederum die erhöhte Stabilität verursachen.

Im vierten Kapitel werden unterschiedliche Oxidationsmedien zur Kohlenstoffentfernung verglichen. Dabei wird die Oxidationskinetik von Ni Nanopartikeln mit zeitaufgelöster Röntgenabsorptionsspektroskopie bestimmt. Eine lineare Korrelation zwischen der Dispersion nach dem Regenerationsvorgang und dem durch die Oxidation des Metalls freiwerdenden Wärmefluss zeigt, dass nur die Oxidation des Metalls für das Wärme-induzierte Sintern relevant ist, und nicht die Oxidation von Kohlenstoff, da diese mit einer sehr viel langsameren Rate abläuft.